# Structural testing and design of wire arc additively manufactured square hollow sections

Pinelopi Kyvelou[1], Cheng Huang[2], Leroy Gardner[3], Craig Buchanan[4]

[1]Research Associate, Dept. of Civil and Environmental Engineering, Imperial College London, South Kensington Campus, London SW7 2AZ, UK. Email:pinelopi.kyvelou11@imperial.ac.uk

[2]Ph.D. Candidate, Dept. of Civil and Environmental Engineering, Imperial College London, South Kensington Campus, London SW7 2AZ, UK (corresponding author). Email: cheng.huang118@imperial.ac.uk

[3]Professor, Dept. of Civil and Environmental Engineering, Imperial College London, South Kensington Campus, London SW7 2AZ, UK. Email: leroy.gardner@imperial.ac.uk

[4]Lecturer, Dept. of Civil and Environmental Engineering, Imperial College London, South Kensington Campus, London SW7 2AZ, UK. Email: craig.buchanan@imperial.ac.uk

**ABSTRACT**

Wire arc additive manufacturing (WAAM) is a method of metal 3D printing that has the potential for significant impact on the construction industry due to its ability to produce large parts, with reasonable printing times and costs. There is currently however a lack of fundamental data on the performance of structural elements produced using this method of manufacture. Seeking to bridge this gap, the compressive behavior and resistance of WAAM square hollow sections (SHS) are investigated in this study. Testing reported in a previous study by the authors of sheet material produced in the same manner as the studied SHS is first summarized. The production, measurement and testing of a series of stainless steel SHS stub columns are then described. Regular cross-section profiles were chosen to isolate the influence of 3D printing and enable direct comparisons to be made against equivalent sections produced using traditional methods of manufacture. A range of cross-section sizes and thicknesses were considered to achieve variation in the local cross-sectional slenderness of the tested specimens, allowing the influence of local buckling to be assessed. Repeat tests enabled the variability in response between specimens to be evaluated; a total of 14 SHS stub columns of seven different local slendernesses was tested, covering all cross-section classes of AISC 370 and Eurocode 3. Advanced non-contact measurement techniques were employed to determine the as-built geometric properties, while digital image correlation measurements were used to provide detailed insight into the deformation characteristics of the test specimens. Owing to the higher geometric variability of WAAM relative to conventional forming processes, the tested 3D printed stub columns were found to exhibit more variable capacities between repeat specimens than is generally displayed by stainless steel SHS. Comparisons of the stub column test results with existing structural design rules highlight the need to allow for the weakening effect of the geometric undulations that are inherent to the WAAM process, in order to achieve safe-sided strength predictions.

**Keywords:** 3D printing; additive manufacturing; digital image correlation; experiments; laser scanning; structural engineering; stub column testing; wire arc additive manufacturing

## 1. INTRODUCTION

Additive manufacturing (AM), also referred to as 3D printing, is a fabrication process where a part is formed through the sequential deposition of layers of material, as dictated by a 3D digital model. The main advantage of this novel method of manufacturing, the use of which has already substantially spread in the aerospace, automotive and biomedical industries (Campbell *et al*., 2012), is the ability to fabricate parts of complex geometry without the need for specific tooling (Hague *et al*., 2004). According to ISO/ASTM 52900 (2015), the principal types of metal AM are sheet lamination, powder bed fusion (PBF) and directed energy deposition (DED). Wire arc additive manufacturing (WAAM) is a method of DED using welding technology, where wire feedstock is melted and selectively deposited onto a substrate plate; the deposited material subsequently solidifies and the desired component is formed layer by layer – see Figure 1 (PAS 6012, 2020). WAAM has the potential for significant impact on the construction industry since it can be used for the production of large-scale parts while allowing for high deposition rates, good structural integrity, reasonable costs and reduced waste material compared to conventional manufacturing processes (Buchanan and Gardner, 2019; Williams *et al*., 2015). Although other metallic AM methods can achieve higher geometrical complexity and accuracy, WAAM allows reduced lead times and manufacturing costs (Lockett *et al*., 2017), using mature technology and wire feedstock of low cost (Thompson *et al*., 2016). Finally, design freedom and printing efficiency can be further enhanced by incorporating multi-axis robotic arms and by adopting multi-direction slicing methodologies, which allow material deposition along multiple directions, thus eliminating the need for supporting structures (Ding *et al*., 2015; Zhang and Liou, 2013).

Although WAAM is offering a revolutionary potential for the construction industry, reliable design guidance on the structural behaviour of metal 3D printed structures is required to enable integration of this new technology to the construction sector. Thus far, structural engineering research has been focused on structural elements printed by other AM methods (Yan *et al*., 2019; Chen *et al*., 2018; Buchanan *et al*., 2017; Yasa, 2011) while experimental data on WAAM structural elements are currently scarce (Laghi *et al*., 2019; Ji *et al*., 2017; Haden *et al*., 2017).

The world's first large-scale demonstrator of WAAM for structural applications is the stainless steel 3D printed bridge shown in Figure 2, constructed by the Dutch start-up company MX3D. The bridge has an overall mass of approximately 7.8 tonnes (of which approximately 4.6 tonnes was printed at a typical deposition rate of 0.5-2.0 kg/h), a span of about 10.5 m and an average width of about 2.5 m (Gardner *et al*., 2020). Being the first of its kind, and featuring material properties and structural behavior beyond the scope of existing design specifications, this novel structure has required extensive experimental and numerical research for its safety to be demonstrated.

A comprehensive experimental programme, comprising material (Kyvelou *et* al., 2020) and cross-sectional tests on tubular sections, has been conducted to support the construction and verification of the MX3D bridge, as well as to explore the potential for wider application of this technology. All tested specimens were printed by MX3D utilising the same feedstock material and printing parameters that were used for the bridge. The destructive experiments were undertaken in the Structures Laboratory in the Department of Civil and Environmental Engineering at Imperial College London while extensive non-destructive physical testing of the bridge has also been undertaken (Gardner *et al.*, 2020).

In this paper, cross-sectional tests on 14 WAAM stub columns of square hollow section (SHS) members, printed using the same material and production parameters as the MX3D bridge, are presented. The process followed for the production, measurement and testing of the stub columns is described while the test results are analysed and discussed. Finally, comparisons are made against the strength predictions of current structural design specifications (AISC 370, 2020; EN1993-1-4, 2020) and against the performance of AM PBF (Buchanan *et al*., 2017) and conventionally formed austenitic (Chen *et al*., 2018; Yuan *et al*., 2014; Gardner and Nethercot, 2004; Rasmussen, 2000; Rasmussen and Hancock, 1993), ferritic (Arrayago *et al*., 2016; Afshan and Gardner, 2013) and duplex (Chen *et al*., 2018; Yuan *et al*., 2014; Theofanous and Gardner, 2009) stainless steel SHS.

## 2. MATERIAL TESTS

In order to determine the stress-strain characteristics of the WAAM material, a comprehensive series of tensile coupon tests was undertaken in a previous study by Kyvelou *et al.* (2020); the key aspects of this study are summarized herein. Dog-bone shaped coupons were extracted from WAAM plates at 0°, 45° and 90° to the printing direction, as defined in Figure 3, to investigate the material anisotropy. The influence of the geometric undulations resulting from the WAAM process on the effective material properties was assessed by testing both as-built and machined coupons; for the machined coupons, all surface undulations were removed using an end mill prior to testing. In total, 39 as-built and 12 machined coupons were tested.

A summary of the average material properties by printing direction (i.e. 0°, 45° and 90°) for the as-built and machined coupons is presented in Tables 1 and 2, respectively, where $\theta$ is the direction of testing relative to the print layer orientation as defined in Figure 3, $t_{\mathrm{nom}}$ is the nominal thickness of the coupon, $E$ is the Young's modulus, $\sigma_{0.2}$ and $\sigma_{1.0}$ are the 0.2% and 1.0% proof stresses respectively, $\sigma_{\mathrm{u}}$ is the ultimate tensile stress, $\varepsilon_{\mathrm{u}}$ is the strain at the ultimate tensile stress and $n$, $m_{1.0}$ and $m_{\mathrm{u}}$ are the strain hardening exponents of the two-stage Ramberg-Osgood material model (Gardner, 2019; Arrayago *et al.*, 2015; Gardner and Ashraf, 2006; Rasmussen, 2003; Mirambell and Real, 2000; Hill, 1944; Ramberg and Osgood, 1943). Note that the mechanical properties of the as-built material are referred to as effective (signified by 'eff' in the subscripts of the symbols) to acknowledge the influence of the undulating geometry. The results highlight the anisotropic behavior of the printed material, while the influence of the irregular geometry on the effective mechanical properties of the WAAM material was shown to be detrimental (and more prominent for loading acting perpendicular to the layer orientation). A more detailed description of the employed test setup and obtained results is provided by Kyvelou *et al.* (2020).

## 3. STUB COLUMN TESTS

Compression tests on WAAM SHS stub columns were conducted to investigate their compressive structural response and load carrying capacity. Simple geometries (i.e. square) were chosen deliberately for the stub column test specimens to enable the influence of the production process alone on the exhibited structural response to be isolated and to allow direct comparisons to be made against traditionally manufactured tubular sections and their corresponding design provisions. Variation in the local cross-section slenderness of the tested specimens was considered by adjusting the cross-sectional proportions (i.e. the outer dimensions and wall thickness), allowing the influence of local buckling to be assessed, while repeated tests enabled the variability in response to be evaluated; 14 SHS stub columns were tested in total.

The adopted labelling system for the test specimens begins with the nominal cross-sectional dimensions in mm (in the form width×depth×thickness), followed by the nominal length in mm and the letter 'F' indicating fixed end conditions; a specimen label ending with an 'R' is a repeat test. Note that specimens 120×120×8.0-450-F and 130×130×3.5-500-F (and their repeats) were chosen to be of similar proportions (i.e. similar width-to-thickness ratios) to key elements of the MX3D bridge. A comparison between specimen 120×120×8.0-450-F and its corresponding part of the substructure of the bridge is shown in Figure 4.

### 3.1 Production and preparation of SHS specimens

The SHS specimens were manufactured by the Dutch start-up company MX3D, using their proprietary multi-axis robotic WAAM technology (MX3D, 2019). The employed printer comprised a 6-axis robotic arm coupled with a metal inert gas (MIG) welding machine. CAD models of the specimens were drawn in Rhino 3D (2017) and sliced into finite layers that the printer could trace along the cross-section slices. Then, wire feedstock, continuously supplied to the printer, was melted and deposited onto a substrate plate, building up the specimen layer by layer. The utilised feedstock material was Grade 308LSi austenitic stainless steel wire. During the deposition process, the current was 100-140 A, the arc voltage was 18-21 V, while the deposition rate was typically between 0.5 and 2.0 kg/h. For the stub columns of 3.5 mm nominal thickness, wire of 1.0 mm diameter was employed with a welding speed of 15- 30 mm/s and a wire feed rate of 4-8 m/min while for the stub columns of 8.0 mm nominal thickness, wire of 1.2 mm diameter was used with a welding speed and wire feed rate of 13 mm/s and 5.7 m/min respectively. Finally, the employed shield gas was 98% AR and 2% $CO_2$, at a flow rate of 10-20 L/min. Printing of typical specimens is illustrated in Figure 5.

Following their fabrication, the stub columns were detached from their substrate plate using a plasma arc cutter and then cut to specified lengths of approximately four times the outer cross-section dimensions; this was chosen to be long enough to include a representative distribution of residual stresses and geometric imperfections, yet short enough to prevent overall flexural buckling (Ziemian, 2010). Both ends of the stub columns were machined to be flat and parallel and the exterior surfaces were sandblasted with glass beads to remove any welding soot from the WAAM process. The cutting process and surface treatment of a typical specimen are shown in Figures 6(a) and 6(b) respectively.

## 3.2 Geometrical measurements

Measuring the geometry of the stub column test specimens was more challenging than usual due to the surface undulations and wall thickness variation arising as a result of the WAAM process. Hand measurements, along with a number of more sophisticated techniques – 3D laser scanning, silicone casting and measurements based on Archimedes' principle – were employed to determine the as-built geometric properties of the SHS specimens. 3D laser scanning and silicone casting were finally adopted, while the hand and Archimedes' measurements served as references for comparison and verification purposes.

### *3.2.1 Hand measurements*

Digital hand calliper measurements were taken to provide baseline geometric data for the examined specimens. Measurements of the SHS face widths (i.e. the outer dimensions $H_h$) were taken at five locations along the length of each specimen (including the two ends), while the wall thickness $t_h$ was recorded at three equally spaced locations on each face, at both ends (i.e. 12 measurements per end in total). Finally, separate length measurements $L_h$ were taken along each SHS face (utilising a tape measure for the longer specimens). The average geometric properties are listed in Table 3, where $A_h$ is the cross-sectional area calculated using the average values of the measurements and with the inner and outer corner radii taken as equal to $1.0t_h$ and $1.5t_h$ respectively, based on hand measurements.

### *3.2.2 Archimedes' principle*

The water displacement method, which is based on Archimedes' physical law of buoyancy and is frequently employed to determine porosity in concrete elements (Ibrahim *et al*. 2014; Park and Tia, 2004) and diffusible hydrogen in welds (Schmid and Rodabaugh, 1980), was utilised for the determination of the average cross-sectional areas of the examined stub columns. Each specimen was hung using chains from weighing scales and its mass was measured both when in air ($m_a$) and when submerged in a water bath ($m_w$); the employed setup is illustrated in Figure 7(a). The mean cross-sectional area of the specimens $A_{Arch}$, reported in Table 3, was hence determined according to Equation (1), by dividing the resulting volume $V_{Arch}$ by the member length $L_h$ (measured as described in Section 3.2.1). In

Equation (1), $m_{c,a}$ and $m_{c,w}$ are the mass of the chain in air and in water (submerged to the same depth as with the specimen hanging) respectively and $\rho_w$ is the density of the water.

$$A_{\text{Arch}} = \frac{V_{\text{Arch}}}{L_h} = \frac{\left[(m_a - m_{c,a}) - (m_w - m_{c,w})\right] / \rho_w}{L_h} \tag{1}$$

*3.2.3 Laser scanning*

In order to obtain an accurate and detailed representation of the external and internal surfaces of all specimens prior to testing, 3D laser scanning was employed. A FARO ScanARM, capable of capturing up to 600,000 points per second to an accuracy of 0.1 mm, was used to scan and digitally reproduce all the printed specimens. Although full scans of the outer surface of the specimens could be taken, the physical size of the head of the laser scan arm prevented direct scanning of the complete inner surface profile (allowing only direct scanning of the inner surface at the column ends) – see Figure 7(b). Hence, silicone casting was undertaken to form a scannable replica of the internal surface of the specimens.

The silicone casts were formed using SUPERSIL 25, a two-component silicone elastomer. The components were thoroughly mixed mechanically and then degassed in a vacuum chamber to remove any entrained air – see Figure 8. A central insert was placed within the specimens, as shown in Figure 9(a), prior to casting to reduce the volume of silicone required and to facilitate easier removal. Silicone release spray was also applied to the inner and outer surfaces of the specimens and inserts respectively. The prepared silicone mixture was then slowly poured in between the insert and the specimen, to avoid the introduction of air voids, which could affect the scanned silicone surface, and allowed to set for at least 24 hours. Once set, the insert was removed, allowing the silicone cast to be collapsed into the void and removed from the printed specimen – see Figure 9(b). A silicone cast adjacent to its parent SHS stub column is shown in Figure 10. Following its extraction from within the specimen, the cured silicone internal replica was laser scanned.

The outer steel and inner silicone scans of the as-built geometries were merged and converted into 3D CAD models with polygon meshes using Geomagic Wrap (2017). The CAD models were subsequently imported into Rhino 3D (2017), where contouring of the specimens was undertaken, allowing accurate determination of the cross-sectional dimensions. Processing of a typical specimen in Rhino is presented in Figure 11, where only a limited number of cross-sectional contours is shown for illustration purposes.

Special attention was given to the determination of the most suitable contour spacing d$x$ along the length of the specimens in order to achieve computational efficiency and accurate determination of the geometric properties. A sensitivity study was therefore undertaken on a typical specimen and its repeat (80×80×3.5-320-F and 80×80×3.5-320-FR), obtaining their geometric measurements at contour spacings of 0.1 mm, 0.2 mm, 0.5 mm, 1.0 mm and 2.0 mm. The obtained results are presented in Figure 12, where the mean, minimum and maximum measurements of the cross-sectional area ($A$, $A_{min}$ and $A_{max}$, respectively) determined for the different contour spacings are normalized against the equivalent values corresponding to d$x$ = 0.1 mm. As expected, the extreme values of the measurements (i.e. $A_{min}$ and $A_{max}$) were more sensitive to the contour spacing compared to the respective mean values (i.e. $A$). Overall, since the measurements obtained using a spacing of 0.2 mm were almost identical to these obtained with a spacing of 0.1 mm, a contour spacing of 0.2 mm was adopted. Note that the considered contour spacings were all below the typical WAAM deposition width $w$, shown in Figure 13, which was found to vary between about 3 mm and 5 mm for the studied specimens; a similar value of 4 mm was reported by Ding *et al*. (2014).

A summary of the geometric properties of all specimens, as obtained from the laser scans, is presented in Table 4, where $t$ and $t_{sd}$ are the mean and standard deviation values of the thickness respectively, $A$, $A_{max}$ and $A_{min}$ are the mean, maximum and minimum cross-sectional areas respectively, $H$ is the average face width and $r$ and $R$ are the inner and outer corner radii, obtained by means of fitting a cylinder to the scanned data of each corner region, as illustrated in Figure 14.

*3.2.4 Comparison between methods*

Comparisons between the geometric properties determined using the different measuring techniques are presented in Table 5. The average cross-sectional areas determined from the hand measurements $A_h$ differ somewhat, ranging between 10% below to 15% above, from those calculated based on Archimedes' principle $A_{Arch}$. This confirms that the use of hand measurements alone can lead to substantial errors in the determination of the geometric properties of WAAM specimens; this is because the discrete hand measurements cannot, in general, be extrapolated to the full sample. Conversely, there is very good agreement between the cross-sectional areas $A_{Arch}$ and $A$, with differences consistently below 3%, providing confidence in the employed 3D laser scanning technique – see Table 5.

### 3.3 Results of geometric measurements

Comparisons between the values of the mean and minimum and mean and maximum cross-sectional areas, as obtained by laser scanning ($A_{min}/A$ and $A_{max}/A$ respectively), are presented in Table 5, revealing the maximum geometric variation within a given specimen. Histograms showing the cross-sectional area variation within specimens are presented in Figure 15, where each cross-sectional area measurement $A_i$ is normalized by the corresponding average cross-sectional area $A$ of each specimen. The values of the coefficient of variation (COV) of the area $V_A$, defined as the ratio of the standard deviation of the area divided by the average area $A_{sd}/A$ of each specimen, are reported in Table 5, and were found to range between 0.04 and 0.10; a similar statistical geometric measure (i.e. $t_{sd}/t$) was used by Kyvelou *et al*. (2020) to predict the influence of the geometric undulations on the effective mechanical properties of WAAM sheet material.

### 3.4 Local geometric imperfections

Determination of the amplitudes of the local geometric imperfections, as distinct from the surface undulations associated with the individual weld layers – see Figure 16, along the length of the examined specimens was undertaken using the points located along the centreline of the outer flat faces (i.e. along one line per face) – see Figure 17. The imperfection amplitude for each face was then defined as the maximum deviation of the selected data points from a straight line fitted to the data using least squares regression. This definition of local imperfection amplitude is considered to be appropriate for evaluating the structural performance of the examined profiles and for use in subsequent numerical analyses, since it is the deviation from flatness along the longitudinal axis of structural elements that triggers and amplifies local instability phenomena (i.e. local plate buckling) and hence governs the ultimate cross-section strength. However, simply using the maximum deviation of the raw data from the reference line was deemed to be inappropriate due to the presence of some particularly prominent surface undulations and pronounced weld beads, which could result in unrealistically large imperfection amplitudes. Therefore, to eliminate the effect of these unwanted features from the data, the obtained imperfection distributions were smoothed to a 10 mm moving average curve, a typical example of which is shown in Figure 18. The 10 mm averaging interval spanned 3 to 4 weld layers and was found, by trial and error, to be suitable for removing the unwanted features, without affecting the underlying imperfection profile; this was the case for all but specimen 100×100×3.5-400-F, where two pronounced weld beads on one of the faces were not fully removed using the moving average approach and hence resulted in unrepresentative imperfection amplitudes; these were therefore removed manually – see Figure 19.

The maximum deviation of the smoothed curves from the reference line among the four faces was then taken as the local imperfection amplitude of each specimen $e_{max}$, as reported in Table 4. The maximum measured imperfection values typically lie between about 0.5 mm and 2.0 mm; these are higher than the imperfection values typically observed in conventionally formed sections (Meng and Gardner, 2020; Schafer and Pekoz, 1998) and similar to the dimensional accuracy of around ± 1.0 mm to ± 2.0 mm generally quoted for WAAM elements (Kumar *et al.*, 2020; Li *et al.*, 2020; Laghi *et al.*, 2019). There was no clear link in the limited dataset between the imperfection amplitude and either the thickness or width of the examined specimens. Note that the largest imperfection amplitude was recorded for specimen 180×180×3.5-720-FR; visual inspection of this specimen confirmed the lower print quality.

A histogram of all 56 local imperfection amplitude measurements (one measurement per section face) is presented in Figure 20, where the cumulative distribution function (CDF) is also plotted. CDF values, along with the key statistics, are given in Table 6. A CDF value, expressed as $P(e_{max,r}<e_{max,d})$, reflects the probability that the maximum geometric imperfection in a randomly selected WAAM specimen $e_{max,r}$ is less than a defined value $e_{max,d}$. The $P(e_{max,r}<e_{max,d}) = 0.95$ (i.e. the characteristic value of the imperfection) corresponds to $e_{max,d} \approx 3.0$ mm, indicating that a WAAM member is expected to have maximum imperfections greater than this value only 5% of the time.

### 3.5 Test setup

The experimental layout adopted for the compressive stub column tests is presented in Figure 21. The load was applied through an Instron 3500 kN testing machine at a displacement rate of 0.5 mm/min while a self-locking spherical head was used to ensure full contact between the stub column ends and end platens. Four equally spaced linear variable displacement transducers (LVDTs) and four strain gauges attached to the specimens at mid-height on opposite faces were used to measure the vertical deformation of the test specimens, while a load cell within the testing machine measured the applied load – this setup has also been used for previous SHS stub column tests (Buchanan *et al.*, 2017; Wang *et al.*, 2017).

Owing to the undulating surface of the examined specimens, a two-component PS polyester adhesive was employed as a surface precoating agent to provide a smooth surface for the attachment of the strain gauges. However, this technique was deemed to provide accurate measurements only up to 0.2% strain, which corresponds to strains substantially lower than those reached during testing. Furthermore, the localised nature of strain gauge readings renders them less representative of the overall structural response in specimens with undulating surfaces; hence, the use of strain gauges was omitted for most of the conducted tests. It should be also mentioned that the testing machine size and the length of specimens 180×180×3.5-720-F and 180×180×3.5-720-FR rendered the use of the self-locking spherical head infeasible; cement grout was used at the top of these specimens instead to ensure full contact between the stub column ends and the loading platen.

Axial load, strain gauge (when used) and LVDT measurements were recorded at a frequency of 2 Hz using an in-house developed data logger. A two camera LaVision DIC system was also used, acquiring images at a frequency of 0.2 Hz, allowing surface deformations and strain fields to be accurately recorded for one of the flat faces of the specimen; the applied force was also recorded through an analogue to digital converter. The acquired images were processed in the software DaVis (LaVision, 2017). Vertical displacements adjacent to the top and bottom end platens were calculated, exported and subtracted to determine the true end shortening response of the stub columns. The surface deformation field of a typical WAAM specimen at the peak load is presented in Figure 22(a) while the equivalent field for a PBF SHS specimen of similar slenderness (Buchanan *et al*., 2017) is shown in Figure 22(b). It can be observed that the deformation field of the WAAM specimen is less regular than for the PBF specimen, especially in terms of out-of-plane deformations. This is attributed to the more variable geometry of the as-built WAAM specimens, particularly the variations in thickness and the surface undulations.

**3.6 Test results**

Two alternative methods were initially adopted for the determination of the load-end shortening curves: (i) using the LVDT and strain gauge data, accounting for the deformation of the end platens (Meng and Gardner, 2020; Zhao *et* al., 2015; Gardner *et al*., 2016; Centre for Advanced Structural Engineering, 1990), and (ii) using the DIC data, by subtracting the vertical deformations recorded at the stub column ends. Typical comparisons between load-end shortening curves derived according to these two different approaches are shown in

Figure 23, where it is apparent that the curves yielded by the two different methods are almost identical. Hence, only the DIC derived results are reported herein since they are deemed to be generally more accurate since the measurements are made directly on the specimens.

The load-end shortening curves of all specimens are presented in Figure 24, while a summary of the obtained results is given in Table 7, where $N_u$ is the ultimate axial load and $\delta_u$ is the column end shortening at $N_u$ as calculated from the DIC data. The deformed shapes of the stub columns, shown in Figure 25, although akin to the classical 'in-out' local buckling, were clearly influenced by the initial imperfections and surface undulations inherent to the WAAM process.

Some variation in structural behavior between repeat specimens was observed, with differences in ultimate capacity up to 18%, reflecting the greater geometric variability associated with WAAM cross-sections relative to conventional sections. In Figure 26(a), the normalized axial resistance $N_u/A\sigma_{0.2,eff}$ of the tested specimens is plotted against the local slenderness $c/(t\varepsilon)$, in order to capture the general trend of decreasing capacity with increasing local slenderness. In Figure 26(a), $c$ is the mean flat width of the faces of the SHS, $t$ is the mean thickness and $\varepsilon = \sqrt{(235/\sigma_{0.2})/(E/210000)}$ (EN 1993-1-4, 2006). In Figure 26(b), the normalized axial resistance $N_u/A\sigma_{0.2,eff}$ of each specimen is itself normalized by the general $N_u/A\sigma_{0.2,eff}$ versus $c/t\varepsilon$ linear regression trend for all tested specimens, the expression for which is denoted $\rho_{linear}$ and given in Figure 26(a), and plotted against the local imperfection amplitude $e_{max}$ (as defined in Section 3.3) normalized by the average thickness $t$. It is clear from the results that the relative structural performance of the WAAM specimens degrades with increasing $e_{max}/t$ values, and that geometric imperfections are the key cause of variation in structural behavior between the repeat tests.

Analysis of the geometric data from the laser scans revealed a general correlation between the location of failure (i.e. local buckling) in the specimens and the regions containing the most prominent thickness reductions and geometric imperfections. In Figure 27, the average wall thickness $t$ and imperfection amplitude $e$ (as defined in Section 3.3) of each cross-section are plotted against the specimen length for two typical specimens (one for each nominal thickness). It can be observed that local buckling is triggered in areas where high values of imperfections and low values of thickness coincide.

# 4. STRUCTURAL DESIGN OF WAAM ELEMENTS

Before broader application of metal 3D printing in the construction sector is possible, further research and greater standardisation is needed. In this section, the performance of the examined WAAM SHS specimens is initially compared against the response of conventionally manufactured SHS, and, subsequently, against strength predictions yielded by design standards of current practice, in order to assess their suitability for the structural design of WAAM SHS.

## 4.1 Comparisons with existing tests data on conventionally manufactured stainless steel SHS

The structural performance of the tested WAAM specimens is compared with that of AM PBF (Buchanan *et al*., 2017) and conventionally formed austenitic (Chen *et al*., 2018; Yuan *et al*., 2014; Gardner and Nethercot, 2004; Rasmussen, 2000; Rasmussen and Hancock, 1993), ferritic (Arrayago *et al*., 2016; Afshan and Gardner, 2013) and duplex (Chen *et al*., 2018; Yuan *et al*., 2014; Theofanous and Gardner, 2009) stainless steel SHS in this sub-section. A graphical illustration is presented in Figure 28, where the normalized axial resistance $N_u/A\sigma_{0.2}$ of the tested specimens is plotted against the local slenderness $c/(t\varepsilon)$, where $c$ is the mean flat width of the faces of the SHS, $t$ is the mean thickness and $\varepsilon = \sqrt{(235/\sigma_{0.2})/(E/210000)}$ (EN 1993-1-4, 2006). Note that, although in the new version of EN 1993-1-4 (2020) the calculation of $\varepsilon$ has been simplified by omitting the $E$/210000 ratio, it has been retained herein because of the significant deviation of the Young's modulus $E$ of the WAAM material from that of traditionally produced material.

Comparisons are shown based on both the machined and effective material properties. It is clear that, when the underlying material properties of the machined coupons are used, the cross-sections under-perform relative to current design provisions. However, when the effective material properties are used, the weakening effect of the geometric undulations, caused by local thickness variations and eccentricities associated with the individual weld layers, is normalized out, and the obtained test results fall within the range of conventionally produced SHS stainless steel stub columns.

## 4.2 Comparisons with AISC 370

In this sub-section, the ultimate test capacities of the WAAM stub columns are compared to the strength predictions determined according to AISC 370 (2020). Two different sets of material properties were utilised in the design equations: (1) the material properties ($E$ and $\sigma_{0.2}$) from the machined coupons in the 90° direction, as reported in Table 2 and (2) the effective material properties ($E_{\text{eff}}$ and $\sigma_{0.2,\text{eff}}$) from the as-built coupons in the 90° direction for both nominal material thicknesses (i.e. 3.5 mm and 8.0 mm), as reported in Table 1. Note that the influence of the geometric undulations associated with WAAM inherently features in the effective material properties determined from the tensile coupon tests performed on the as-built material. The capacity predictions derived using the two different sets of material properties are denoted $N_{\text{u,AISC,m}}$ and $N_{\text{u,AISC,eff}}$ respectively. The mean cross-sectional dimensions, as determined from the laser scans, were used in all design calculations and all safety factors were set to unity.

Comparisons between the test results and AISC 370 strength predictions are presented in Figure 29 and listed in Table 8. Note that, although the reduction factor accounting for local buckling is used in the design equations to reduce only the flat widths of the SHS faces (and not the gross cross-sectional area), in Figure 29, for illustration purposes, the AISC 370 reduction factor function has been directly plotted. It can be observed that use of the material properties obtained from the machined coupons leads to consistent overpredictions of the load-carrying capacities of the examined cross-sections (with $N_{\text{u}}/N_{\text{u,AISC,m}} = 0.85$ on average), while use of the effective material properties leads to more reasonable and safe-sided resistance predictions (with $N_{\text{u}}/N_{\text{u,AISC,eff}} = 1.12$ on average). Hence, it is clear that account of the weakening effect of geometric undulations should be taken (for example through the use of effective material properties as adopted herein or through an alternative reduced thickness approach) to achieve suitable strength predictions using the AISC 370 resistance function, but further data and reliability analyses are required before a suitable safety factor could be derived.

### 4.3 Comparisons with EN 1993-1-4

In this sub-section, the ultimate test capacities of the WAAM stub columns are compared to the resistance predictions determined according to EN 1993-1-4 (2020). The comparisons are illustrated in Figure 30 and are presented in Table 9, together with the compressive cross-section classes. As in Section 4.2, use of the material properties from both the machined and as-built coupons for the 90° direction has been assessed in the EN 1993-1-4 resistance function; the resulting resistance predictions are denoted $N_{\text{u,EN,m}}$ and $N_{\text{u,EN,eff}}$ respectively. Note that effective cross-sectional properties have been calculated for Class 4 sections in line with EN 1993-1-4 (2020) and EN 1993-1-5 (2006) to account for the loss of effectiveness due to local buckling while $\varepsilon$ was calculated as explained in Section 4.1 (i.e. $\varepsilon = \sqrt{(235/\sigma_{0.2})/(E/210000)}$). Also, as for the AISC 370 comparisons, although the reduction factor accounting for local buckling $\rho$ is only used to reduce the flat widths of the SHS faces (and not the gross cross-sectional area), in Figure 30, for illustration purposes, the EN 1993-1-4 reduction factor function has been directly plotted.

It is clear that, when the underlying material properties of the machined coupons are used, the load-carrying capacities of the examined cross-sections are generally overpredicted (with $N_u/N_{u,EN,m}$ = 0.85 on average). Conversely, when the effective material properties of the undulating coupons are employed, more reasonable resistance predictions are achieved (with $N_u/N_{u,EN,eff}$=1.13 on average). Hence, as for AISC 370, provided the weakening effect of the undulations inherent in the as-built geometry is considered (through the use of effective mechanical properties in the present study), adequate resistance predictions for WAAM SHS in compression are achieved using the existing EN 1993-1-4 (2020) design equations. Again, further data and reliability analyses are required before a suitable safety factor could be derived.

### 4.4 Comparisons with the continuous strength method

The continuous strength method (CSM) (Arrayago *et al.*, 2020; Afshan and Gardner, 2013; Gardner *et al.*, 2011) has been also used to predict the cross-sectional resistances of the tested WAAM specimens. The CSM, which has been recently included in both AISC 370 (2020) and EN 1993-1-4 (2020), is a deformation-based design approach that accounts for the beneficial influence of strain hardening. The CSM capacities predicted using the material properties of the machined and as-built coupons are denoted $N_{u,csm,m}$ and $N_{u,csm,eff}$ respectively. Normalized CSM resistance predictions are provided in Table 10 and illustrated in Figure 31 (where the CSM prediction curve has been plotted using the effective material properties of the 3.5 mm specimens), with $N_u/N_{u,csm,m}$ = 0.76 and $N_u/N_{u,csm,eff}$ = 1.00 on average. The CSM resistance predictions are accurate when the effective material properties of the as-built coupons are employed, but may, nonetheless, require recalibration for application to WAAM structural elements in order to ensure that the required level of reliability is achieved.

## 5. CONCLUSIONS

An experimental study into the material and cross-sectional properties of WAAM stainless steel structural elements has been presented. The research was carried out to gain insight into the structural behavior of WAAM stainless steel members and, also, to complement the safety verification of the world's first metal 3D printed bridge (Gardner *et al*., 2020).

Compression tests on a total of 14 SHS stub columns, covering a wide range of local slendernesses, were performed. Sophisticated non-contact measurement techniques were employed to determine the as-built geometric properties of the specimens, featuring 3D laser scanning, silicone casting and measurements based on Archimedes' principle, while digital image correlation measurements were used to provide detailed insight into the deformation characteristics of the test specimens. It was found that the WAAM stub columns exhibited more variable capacities between repeat specimens than generally displayed by conventionally formed stainless steel SHS and this was demonstrated to relate principally to the variation in local geometric imperfections.

The test results were compared with capacity predictions obtained using the AISC 370, EN 1993-1-4 and CSM resistance functions with mechanical properties determined from tensile tests on both machined and as-built WAAM coupons, with the latter including the weakening effect of the undulating geometry inherent to the WAAM process. Use of the machined material properties generally resulted in unconservative capacity predictions, while this was remedied through the use of the effective mechanical properties of the as-built coupons. Further test data and reliability analyses are required for the determination of suitable safety factors for the design of cross-sections produced by wire arc additive manufacturing.

## DATA AVAILABILITY STATEMENT

Some or all data, models, or code that support the findings of this study are available from the corresponding author upon reasonable request.

## ACKNOWLEDGEMENTS

This experimental programme was possible thanks to funding and support from the Data Centric Engineering programme at the Alan Turing Institute (ATI), funded by the Lloyd's Register Foundation. This research also benefitted from EPSRC funding under grant number EP/R010161/1 and from the UKCRIC Coordination Node EPSRC grant under EP/R017727/1. The authors would also like to acknowledge the contributions of William

Sharpe, Rory Jones, Wing Wan, Anna Schumacher, Tim Lui, Gordon Herbert, Paul Crudge, Trevor Stickland, Les Clark, Alfredo Olivo, Dave de Ruyter and the late Ron Millward from the Department of Civil and Environmental Engineering and of Ingrid Logan and Saadiqah Rahman from the Dyson School of Design Engineering at Imperial College London in the conducted experimental programme.

## REFERENCES

3D Systems (2017) *Geomagic Wrap 2017* (Version 2017.0.2:64) [Software] 2017 3D Systems, Incorporated and its licensors.

Afshan, S. and Gardner, L. (2013) Experimental Study of Cold-Formed Ferritic Stainless Steel Hollow Sections. *Journal of Structural Engineering*, 139 (5), 717-728.

Afshan, S. and Gardner, L. (2013) The continuous strength method for structural stainless steel design. *Thin-Walled Structures*, 68, 42-49.

AISC 370 (2020) *Specification for Structural Stainless Steel Buildings*. Chicago, Illinois, American Institute of Steel Construction.

Arrayago, I., Real, E. and Gardner, L. (2015) Description of stress-strain curves for stainless steel alloys. *Materials and Design*, 87, 540-552.

Arrayago, I., Real, E. and Mirambell, E. (2016) Experimental study on ferritic stainless steel RHS and SHS beam-columns. *Thin-Walled Structures*, 100, 93-104.

Arrayago, I., Real, E., Mirambell, E. and Gardner, L. (2020) The Continuous Strength Method for the design of stainless steel hollow section columns. *Thin-Walled Structures*, 154, 106825.

Buchanan, C. and Gardner, L. (2019) Metal 3D printing in construction: a review of methods, research, applications, opportunities and challenges. *Engineering Structures*, 180, 332-348.

Buchanan, C., Matilainen, V.P., Salminen, A. and Gardner, L. (2017) Structural performance of additive manufactured metallic material and cross-sections. *Journal of Constructional Steel Research*, 136, 35-48.

Campbell, I., Bourell, D. and Gibson I. (2012). Additive Manufacturing: rapid prototyping comes of age. *Rapid Prototyping Journal*, 18 (4), 255-258.

Centre for Advanced Structural Engineering (1990) Compression tests of stainless steel tubular columns. *Investigation Report S770*. University of Sydney, Australia.

Chen, J., Huang, Y. and Young, B. (2019) Design of austenitic and duplex stainless steel SHS and RHS beam-columns. *Journal of Constructional Steel Research*, 152, 143-153.

Chen, M.T., Yan, J.J., Quach, W.M., Yan, M. and Young, B. (2018) Additive Manufactured High Strength Steel Tubular Sections. In: *Proceedings of the 8th International Conference on Thin-Walled Structures (ICTWS)*: 1-24. 24-27 July, Lisbon, Portugal.

Ding, D. H., Pan, Z. X., Dominic, C. and Li, H. J. (2014) Process planning strategy for wire and arc additive manufacturing. *International Conference on Robotic Welding, Intelligence and Automation*. Springer, 437-450.

EN 1993-1-4 (2020) *Eurocode 3: Design of Steel Structures - Part 1–4: General Rules - Supplementary Rules for Stainless Steels*. Brussels, European Committee for Standardization (CEN).

EN 1993-1-4 (2006) *Eurocode 3: Design of Steel Structures - Part 1–4: General Rules - Supplementary Rules for Stainless Steels*. Brussels, European Committee for Standardization (CEN).

EN 1993-1-5 (2006) *Eurocode 3: Design of Steel Structures - Part 1–5: Plated structural elements*. Brussels, European Committee for Standardization (CEN).

EN ISO 6892- 1 (2016) *Metallic materials - Tensile testing – Part 1: Method of test at room temperature*. Brussels, European Committee for Standardization (CEN).

Gardner, L. (2019) Stability and design of stainless steel structures – Review and outlook. *Thin-Walled Structures*, 141, 208-216.

Gardner, L. and Ashraf, M. (2006) Structural design for non-linear metallic materials. *Engineering Structures*, 28 (6), 926-934.

Gardner, L., Bu, Y. and Theofanous, M. (2016) Laser-welded stainless steel I-sections: Residual stress measurements and column buckling tests. *Engineering Structures*, 127, 536-548.

Gardner, L., Kyvelou P., Herbert, G. and Buchanan, C. (2020) Testing and initial verification of the world's first metal 3D printed bridge. *Journal of Constructional Steel Research*, 172, 106233.

Gardner, L. and Nethercot, D.A. (2004) Experiments on stainless steel hollow sections – part 1: material and cross-sectional behaviour. *Journal of Constructional Steel Research*, 60 (9), 1291-1318.

Gardner, L., Wang, F. and Liew, A. (2011) Influence of strain hardening on the behavior and design of steel structures. *International Journal of Structural Stability and Dynamics*, 11 (5), 855-875.

Haden, C., Zeng, G., Carter III, F. M., Ruhl, C., Krick, B. and Harlow, D. (2017). Wire and arc additive manufactured steel: tensile and wear properties. *Additive Manufacturing*, 16, 115-123.

Hague, R., Mansour, S. and Saleh, N. (2004) Material and design considerations for rapid manufacturing. *International Journal of Production Research*, 42 (22), 4691-4708.

Hill, H. (1944) Determination of stress-strain relations from the offset yield strength values. *Technical Note No. 927, National Advisory Committee for Aeronautics*. Washington, D.C., USA.

Ibrahim, A., Mahmoud, E., Yamin, M. and Patibandla, V.C. (2014) Experimental study on Portland cement pervious concrete mechanical and hydrological properties. *Construction and Building Materials*, 50, 524-529.

ISO/ASTM 52900 (2015) *Additive Manufacturing – General Principles – Terminology*. ASTM International, West Conshohocken, PA.

Ji, L., Lu, J., Liu, C., Jing, C., Fan, H. and Ma, S. (2017) Microstructure and mechanical properties of 304l steel fabricated by arc additive manufacturing. *MATEC Web of Conferences*, 128 (EDP Sciences), 03006.

Kumar, P., Jain, N.K. and Sawant, M.S. (2020) Modeling of dimensions and investigations on geometrical deviations of metallic components manufactured by μ-plasma transferred arc additive manufacturing process. *The International Journal of Advanced Manufacturing Technology*, 7-8 (107), 3155-3168.

Kyvelou, P., Slack, H., Daskalaki Mountanou, D., Wadee, M.A., Britton, T.B., Buchanan, C. and Gardner, L. (2020) Mechanical and microstructural testing of WAAM sheet material. *Materials and Design*, 192, 108675.

Laghi, V., Palermo, M., Gasparini, G., Girelli, V. and Trombetti, T. (2019) Experimental results for structural design of Wire-and-Arc Additive Manufactured stainless steel members. *Journal of Constructional Steel Research*. [In press]

LaVision (2017) *DaVis* (Version 8.4.0) [Software] La Vision GmbH.

Lockett, H., Ding, J., Williams, S. and Martina, F. (2017) Design for Wire + Arc Additive Manufacture: design rules and build orientation selection. *Journal for Engineering Design*, 28 (7-9), 568-598.

Li, Y., Li, X., Zhang, G., Horváth, I. and Han, Q. (2020) Interlayer closed-loop control of forming geometries for wire and arc additive manufacturing based on fuzzy-logic inference. *Journal of Manufacturing Processes*. [In press]

Meng, X. and Gardner, L. (2020) Testing of hot-finished high strength steel SHS and RHS under combined compression and bending. *Thin-Walled Structures*, 148, 106262.

Mirambell, E. and Real, E. (2000) On the calculation of deflections in structural stainless steel beams: an experimental and numerical investigation. *Journal of Constructional Steel Research*, 54 (1), 109-133.

MX3D (2019) About - MX3D. [online] Available from: https://mx3d.com/about-2/ [Accessed 18 Oct. 2019]

Park, S.B. and Tia, M. (2004) An experimental study on the water-purification properties of porous concrete. *Cement and Concrete Research*, 34, 177-184.

PAS 6012 (2020) *Additive manufacturing – Wire arc – Guide*. The British Standards Institution (BSI).

Ramberg, W. and Osgood, W.R. (1943) Description of stress-strain curves by three parameters. *Technical Note No. 902, National Advisory Committee for Aeronautics*. Washington, D.C., USA.

Rasmussen, K. J. R. (2003) Full-range stress-strain curves for stainless steel alloys. *Journal of Constructional Steel Research*, 59 (1), 47-61.

Rasmussen, K.J.R. (2000) Recent research on stainless steel tubular structures. *Journal of Constructional Steel Research*, 54 (1), 75-88.

Rasmussen, K.J.R. and Hancock, G.J. (1993) Design of cold-formed stainless steel tubular members. I: columns. *Journal of Structural Engineering*. *ASCE*, 119 (8), 2349-2367.

Rhino 3D. (2017) *Rhino 3D computer-aided design software* (Version 5 SR14 64-bit) [Software] Robert McNeel & Associates.

Ryan, E. M. (2019) *On wire and arc additive manufacture of aluminium*. PhD thesis. University of Surrey, UK.

Schafer, B.W. and Pekoz, T. (1998) Computational modeling of cold-formed steel: characterizing geometric imperfections and residual stresses. *Journal of Constructional Steel Research*, 47, 193-210.

Schmid, G.C. and Rodabaugh, R.D. (1980) Water displacement method for measuring diffusible hydrogen in welds. *Welding Journal*, 59 (8), 217-225.

Theofanous, M. and Gardner, L. (2009) Testing and numerical modelling of lean duplex stainless steel hollow section columns. *Engineering Structures*, 31, 3047-3058.

Thompson, M.K., Moroni, G., Vaneker, T., Fadel, G., Campbell, R.I., Gibson, I., Bernard, A., Schulz, J., Graf, P., Ahuja, B. and Martina, F. (2016) Design for Additive Manufacturing: Trends, opportunities, considerations, and constraints. *CIRP Annals – Manufacturing Technology*, 65 (2), 737-760.

Wang, J., Afshan, S., Schillo, N., Theofanous, M., Feldmann, M. and Gardner, L. (2017) Material properties and compressive local buckling response of high strength steel square and rectangular hollow sections. *Engineering Structures*, 130, 297-315.

Williams, S.W., Martina, F., Addison, A.C., Ding, J., Pardal, G. and Colegrove, P.A. (2015) Wire + Arc Additive Manufacturing. *Materials Science and Technology*, 32 (7), 641-647.

Yan, J.-J., Chen, M.-T., Quach, W.-M., Yan, M. and Young, B. (2019) Mechanical properties and cross-sectional behavior of additively manufactured high strength steel tubular sections. *Thin-Walled Structures*, 144, 106158.

Yasa, E. and Kruth, J-P. (2011) Microstructural investigation of Selective Laser Melting 316L stainless steel parts exposed to laser re-melting. *Procedia Engineering*, 19, 389-395.

Yuan, H.X., Wang, Y.Q., Shi, Y.J. and Gardner, L. (2014) Stub column tests on stainless steel built-up sections. *Thin-Walled Structures*, 83, 103-114.

Zhang, J. and Liou, F.W. (2013) Multi-Axis Planning of a Hybrid Material Deposition and Removal Combined Process. *Journal of Machinery Manufacturing and Automation*, 2 (3), 46-57.

Zhao, O., Rossi, B., Gardner, L. and Young, B. (2015) Behaviour of structural stainless steel cross-sections under combined loading – Part I: Experimental study. *Engineering Structures*, 89, 236-246.

Ziemian, R.D. (2010) *Guide to Stability Design Criteria for Metal Structures*. 6th edition. New York, John Wiley & Sons, Inc.

## TABLES

Table 1: Average effective material properties of as-built coupons by direction of testing relative to the print layer orientation (Kyvelou *et al*., 2020)

| $t_{nom}$ (mm) | $\theta$ (°) | $E_{eff}$ (MPa) | $\sigma_{0.2,eff}$ (MPa) | $\sigma_{1.0,eff}$ (MPa) | $\sigma_{u,eff}$ (MPa) | $\varepsilon_{u,eff}$ | $n_{eff}$ | $m_{1.0,eff}$ | $m_{u,eff}$ |
|---|---|---|---|---|---|---|---|---|---|
| 3.5 | 0 | 135900 | 333 | 362 | 553 | 0.273 | 15.5 | 1.8 | 2.2 |
| | 45 | 192600 | 344 | 391 | 570 | 0.255 | 9.4 | 2.4 | 2.3 |
| | 90 | 90200 | 261 | 319 | 448 | 0.119 | 6.5 | 2.5 | 2.6 |
| 8.0 | 0 | 137100 | 325 | 349 | 535 | 0.325 | 22.9 | 1.8 | 2.4 |
| | 45 | 201200 | 351 | 391 | 559 | 0.255 | 11.5 | 2.3 | 2.3 |
| | 90 | 109100 | 271 | 326 | 423 | 0.103 | 5.5 | 2.6 | 2.5 |

Table 2: Average material properties of machined coupons by direction of testing relative to the print layer orientation (Kyvelou *et al*., 2020)

| $\theta$ (°) | $E$ (MPa) | $\sigma_{0.2}$ (MPa) | $\sigma_{1.0}$ (MPa) | $\sigma_u$ (MPa) | $\varepsilon_u$ | $n$ | $m_{1.0}$ | $m_u$ |
|---|---|---|---|---|---|---|---|---|
| 0 | 143300 | 356 | 382 | 575 | 0.307 | 15.8 | 1.7 | 2.4 |
| 45 | 219500 | 407 | 437 | 626 | 0.364 | 13.6 | 2.0 | 2.4 |
| 90 | 139600 | 338 | 381 | 554 | 0.297 | 6.8 | 2.3 | 2.7 |

Table 3: Summary of the average hand measured geometric properties of the SHS specimens

| Specimen ID | $L_h$ (mm) | $H_h$ (mm) | $t_h$ (mm) | $A_h$ (mm$^2$) | $A_{Arch}$ (mm$^2$) |
|---|---|---|---|---|---|
| 60×60×3.5-240-F | 240.1 | 59.7 | 3.91 | 857.1 | 888.3 |
| 60×60×3.5-240-FR | 240.3 | 60.0 | 3.82 | 841.8 | 838.8 |
| 80×80×3.5-320-F | 320.4 | 80.0 | 3.86 | 1160.5 | 1191.9 |
| 80×80×3.5-320-FR | 320.0 | 79.9 | 3.80 | 1140.9 | 1153.4 |
| 100×100×3.5-400-F | 400.4 | 100.0 | 4.31 | 1627.8 | 1516.8 |
| 100×100×3.5-400-FR | 409.3 | 100.0 | 4.39 | 1657.4 | 1499.2 |
| 120×120×8.0-450-F | 475.4 | 119.2 | 7.23 | 3181.7 | 2876.5 |
| 120×120×8.0-450-FR | 450.9 | 119.1 | 7.04 | 3101.8 | 2700.9 |
| 130×130×3.5-500-F | 501.6 | 131.0 | 3.96 | 1994.1 | 1840.9 |
| 130×130×3.5-500-FR | 487.5 | 130.6 | 4.35 | 2176.6 | 1829.1 |
| 150×150×3.5-600-F | 600.0 | 149.6 | 3.88 | 2247.8 | 2285.4 |
| 150×150×3.5-600-FR | 599.5 | 149.8 | 3.98 | 2304.7 | 2271.2 |
| 180×180×3.5-720-F | 720.0 | 179.4 | 3.96 | 2761.0 | 2765.3 |
| 180×180×3.5-720-FR | 720.3 | 179.1 | 3.59 | 2503.8 | 2790.1 |

Table 4: Summary of the average geometric properties of the SHS specimens as determined by the laser scans and by measurements based on Archimedes' principle

| Specimen ID | $H$ (mm) | $r$ (mm) | $R$ (mm) | $t$ (mm) | $A$ (mm$^2$) | $A_{max}$ (mm$^2$) | $A_{min}$ (mm$^2$) | $e_{max}$ (mm) |
|---|---|---|---|---|---|---|---|---|
| 60×60×3.5-240-F | 60.0 | 4.48 | 7.15 | 4.11 | 914.8 | 1116.0 | 795.1 | 1.41 |
| 60×60×3.5-240-FR | 60.0 | 4.76 | 7.19 | 3.85 | 843.6 | 969.2 | 750.6 | 1.39 |
| 80×80×3.5-320-F | 79.9 | 4.46 | 7.11 | 4.05 | 1227.4 | 1544.6 | 1069.0 | 1.65 |
| 80×80×3.5-320-FR | 80.0 | 4.49 | 7.15 | 3.91 | 1182.2 | 1332.6 | 1052.5 | 2.05 |
| 100×100×3.5-400-F | 100.0 | 4.32 | 6.54 | 3.99 | 1496.7 | 1703.2 | 1372.2 | 0.62 |
| 100×100×3.5-400-FR | 99.9 | 4.29 | 6.79 | 3.99 | 1520.2 | 1699.0 | 1355.3 | 0.72 |
| 120×120×8.0-450-F | 118.0 | 5.60 | 8.11 | 6.53 | 2894.2 | 3217.2 | 2495.1 | 1.78 |
| 120×120×8.0-450-FR | 117.1 | 5.28 | 8.09 | 6.27 | 2709.9 | 3417.9 | 2426.8 | 2.69 |
| 130×130×3.5-500-F | 129.0 | 4.92 | 7.35 | 3.62 | 1848.8 | 2149.3 | 1652.0 | 1.53 |
| 130×130×3.5-500-FR | 128.8 | 4.96 | 7.73 | 3.64 | 1824.2 | 2340.3 | 1636.4 | 1.41 |
| 150×150×3.5-600-F | 149.8 | 4.37 | 6.67 | 4.05 | 2324.1 | 2633.8 | 2009.5 | 1.14 |
| 150×150×3.5-600-FR | 149.7 | 4.22 | 7.11 | 4.00 | 2327.1 | 2737.4 | 1910.5 | 0.71 |
| 180×180×3.5-720-F | 179.5 | 4.45 | 6.73 | 4.05 | 2832.3 | 3248.9 | 2419.5 | 1.13 |
| 180×180×3.5-720-FR | 179.0 | 4.65 | 6.87 | 4.06 | 2874.1 | 4849.2 | 2380.8 | 3.80 |

Table 5: Comparison of geometric properties determined using different measurement methods

| Specimen ID | $A_h$ / $A_{Arch}$ | $A$ / $A_{Arch}$ | $A$ / $A_{min}$ | $A$ / $A_{max}$ | $A_{sd}$ / $A$ | $e_{max}$ / $t$ |
|---|---|---|---|---|---|---|
| 60×60×3.5-240-F | 0.96 | 1.03 | 1.15 | 0.82 | 0.07 | 0.34 |
| 60×60×3.5-240-FR | 1.00 | 1.01 | 1.12 | 0.87 | 0.06 | 0.36 |
| 80×80×3.5-320-F | 0.97 | 1.03 | 1.15 | 0.79 | 0.07 | 0.41 |
| 80×80×3.5-320-FR | 0.99 | 1.02 | 1.12 | 0.89 | 0.05 | 0.52 |
| 100×100×3.5-400-F | 1.07 | 0.99 | 1.09 | 0.88 | 0.04 | 0.16 |
| 100×100×3.5-400-FR | 1.11 | 1.01 | 1.12 | 0.89 | 0.05 | 0.18 |
| 120×120×8.0-450-F | 1.11 | 1.01 | 1.16 | 0.90 | 0.04 | 0.27 |
| 120×120×8.0-450-FR | 1.15 | 1.00 | 1.12 | 0.79 | 0.05 | 0.43 |
| 130×130×3.5-500-F | 1.08 | 1.00 | 1.12 | 0.86 | 0.05 | 0.42 |
| 130×130×3.5-500-FR | 1.19 | 1.00 | 1.11 | 0.78 | 0.08 | 0.39 |
| 150×150×3.5-600-F | 0.98 | 1.02 | 1.16 | 0.88 | 0.05 | 0.28 |
| 150×150×3.5-600-FR | 1.01 | 1.02 | 1.22 | 0.85 | 0.04 | 0.18 |
| 180×180×3.5-720-F | 1.00 | 1.02 | 1.17 | 0.87 | 0.04 | 0.28 |
| 180×180×3.5-720-FR | 0.90 | 1.03 | 1.21 | 0.59 | 0.10 | 0.94 |
| Mean | 1.04 | 1.01 | 1.14 | 0.83 | 0.06 | 0.37 |
| COV | 0.08 | 0.01 | 0.03 | 0.09 | 0.29 | 0.51 |

Table 6: Cumulative distribution function (CDF) values for imperfection amplitudes

| P ($e_{max,r}$ < $e_{max,d}$) | $e_{max}$ (mm) |
|---|---|
| 0.25 | 0.73 |
| 0.50 | 1.28 |
| 0.75 | 1.50 |
| 0.90 | 2.05 |
| 0.95 | 2.94 |
| 0.99 | 3.80 |
| Mean | 1.29 |
| St. Dev. | 0.68 |

Table 7: Summary of stub column test results

| Specimen ID | $N_u$ (kN) | $\delta_u$ (mm) |
|---|---|---|
| 60×60×3.5-240-F | 277.5 | 5.84 |
| 60×60×3.5-240-FR | 250.6 | 5.74 |
| 80×80×3.5-320-F | 353.0 | 3.69 |
| 80×80×3.5-320-FR | 314.1 | 3.25 |
| 100×100×3.5-400-F | 440.8 | 2.86 |
| 100×100×3.5-400-FR | 437.6 | 2.81 |
| 120×120×8.0-450-F | 993.2 | 8.86 |
| 120×120×8.0-450-FR | 841.1 | 6.64 |
| 130×130×3.5-500-F | 437.4 | 2.23 |
| 130×130×3.5-500-FR | 414.8 | 1.87 |
| 150×150×3.5-600-F | 520.3 | 2.27 |
| 150×150×3.5-600-FR | 556.1 | 2.34 |
| 180×180×3.5-720-F | 528.1 | 1.89 |
| 180×180×3.5-720-FR | 468.1 | 2.26 |

Table 8: Comparisons of test results with AISC 370 design predictions

| | Test | AISC 370 predictions (machined properties) | | | AISC 370 predictions (effective properties) | | | Comparisons | |
|---|---|---|---|---|---|---|---|---|---|
| Specimen ID | $N_u$ (kN) | Class | $\lambda\sqrt{\sigma_{0.2}/E}$ | $N_{u,AISC,m}$ (kN) | Class | $\lambda\sqrt{\sigma_{0.2}/E}$ | $N_{u,AISC,eff}$ (kN) | $N_u$ / $N_{u,AISC,m}$ | $N_u$ / $N_{u,AISC,eff}$ |
| 60×60×3.5-240-F | 277.5 | Non slender | 0.53 | 309.2 | Non slender | 0.58 | 238.8 | 0.90 | 1.16 |
| 60×60×3.5-240-FR | 250.6 | Non slender | 0.56 | 285.1 | Non slender | 0.62 | 220.2 | 0.88 | 1.14 |
| 80×80×3.5-320-F | 353.0 | Non slender | 0.78 | 414.9 | Non slender | 0.85 | 320.4 | 0.85 | 1.10 |
| 80×80×3.5-320-FR | 314.1 | Non slender | 0.81 | 399.6 | Non slender | 0.89 | 308.6 | 0.79 | 1.02 |
| 100×100×3.5-400-F | 440.8 | Non slender | 1.05 | 505.9 | Non slender | 1.15 | 390.6 | 0.87 | 1.13 |
| 100×100×3.5-400-FR | 437.6 | Non slender | 1.05 | 513.8 | Non slender | 1.14 | 396.8 | 0.85 | 1.10 |
| 120×120×8.0-450-F | 993.2 | Non slender | 0.74 | 978.2 | Non slender | 0.75 | 784.3 | 1.02 | 1.27 |
| 120×120×8.0-450-FR | 841.1 | Non slender | 0.76 | 915.9 | Non slender | 0.77 | 734.4 | 0.92 | 1.15 |
| 130×130×3.5-500-F | 437.4 | Slender | 1.54 | 534.7 | Slender | 1.68 | 386.3 | 0.82 | 1.13 |
| 130×130×3.5-500-FR | 414.8 | Slender | 1.52 | 530.8 | Slender | 1.66 | 383.2 | 0.78 | 1.08 |
| 150×150×3.5-600-F | 520.3 | Slender | 1.64 | 632.7 | Slender | 1.79 | 454.7 | 0.82 | 1.14 |
| 150×150×3.5-600-FR | 556.1 | Slender | 1.65 | 631.3 | Slender | 1.81 | 454.3 | 0.88 | 1.22 |
| 180×180×3.5-720-F | 528.1 | Slender | 2.00 | 656.5 | Slender | 2.18 | 471.4 | 0.80 | 1.12 |
| 180×180×3.5-720-FR | 468.1 | Slender | 1.98 | 675.7 | Slender | 2.16 | 486.0 | 0.69 | 0.96 |
| | | | | | | | Mean | 0.85 | 1.12 |
| | | | | | | | COV | 0.09 | 0.06 |

Table 9: Comparisons of test results with EN 1993-1-4 design predictions

| Specimen ID | Test | EN1993-1-4 predictions (machined properties) | | | EN1993-1-4 predictions (effective properties) | | | Comparisons | |
|---|---|---|---|---|---|---|---|---|---|
| | $N_u$ (kN) | Class | $c/(t\varepsilon)$ | $N_{u,EN,m}$ (kN) | Class | $c/(t\varepsilon)$ | $N_{u,EN,eff}$ (kN) | $N_u$ / $N_{u,EN,m}$ | $N_u$ / $N_{u,EN,eff}$ |
| 60×60×3.5-240-F | 277.5 | 1 | 15.8 | 309.2 | 1 | 17.3 | 238.8 | 0.90 | 1.16 |
| 60×60×3.5-240-FR | 250.6 | 1 | 16.9 | 285.1 | 1 | 18.5 | 220.2 | 0.88 | 1.14 |
| 80×80×3.5-320-F | 353.0 | 1 | 23.3 | 414.9 | 1 | 25.5 | 320.4 | 0.85 | 1.10 |
| 80×80×3.5-320-FR | 314.1 | 1 | 24.3 | 399.6 | 1 | 26.5 | 308.6 | 0.79 | 1.02 |
| 100×100×3.5-400-F | 440.8 | 1 | 31.4 | 505.9 | 2 | 34.3 | 390.6 | 0.87 | 1.13 |
| 100×100×3.5-400-FR | 437.6 | 1 | 31.3 | 513.8 | 2 | 34.2 | 396.8 | 0.85 | 1.10 |
| 120×120×8.0-450-F | 993.2 | 1 | 22.0 | 978.2 | 1 | 22.3 | 784.3 | 1.02 | 1.27 |
| 120×120×8.0-450-FR | 841.1 | 1 | 22.9 | 915.9 | 1 | 23.2 | 734.4 | 0.92 | 1.15 |
| 130×130×3.5-500-F | 437.4 | 4 | 45.9 | 532.0 | 4 | 50.2 | 384.6 | 0.82 | 1.14 |
| 130×130×3.5-500-FR | 414.8 | 4 | 45.4 | 528.2 | 4 | 49.7 | 381.4 | 0.79 | 1.09 |
| 150×150×3.5-600-F | 520.3 | 4 | 48.9 | 629.6 | 4 | 53.5 | 452.7 | 0.83 | 1.15 |
| 150×150×3.5-600-FR | 556.1 | 4 | 49.4 | 628.3 | 4 | 54.0 | 452.4 | 0.89 | 1.23 |
| 180×180×3.5-720-F | 528.1 | 4 | 59.6 | 653.9 | 4 | 65.2 | 469.6 | 0.81 | 1.12 |
| 180×180×3.5-720-FR | 468.1 | 4 | 59.2 | 673.0 | 4 | 64.7 | 484.3 | 0.70 | 0.97 |
| | | | | | | | Mean | 0.85 | 1.13 |
| | | | | | | | COV | 0.08 | 0.06 |

Table 10: Comparisons of test results with CSM design predictions

| Specimen ID | Test | CSM predictions (machined properties) | | | CSM predictions (effective properties) | | | Comparisons | |
|---|---|---|---|---|---|---|---|---|---|
| | $N_u$ (kN) | $\bar{\lambda}_{p,cs}$ | $\varepsilon_{csm}/\varepsilon_y$ | $N_{u,csm,m}$ (kN) | $\bar{\lambda}_{p,cs}$ | $\varepsilon_{csm}/\varepsilon_y$ | $N_{u,csm,eff}$ (kN) | $N_u$ / $N_{u,csm,m}$ | $N_u$ / $N_{u,csm,eff}$ |
| 60×60×3.5-240-F | 277.5 | 0.28 | 15.00 | 420.9 | 0.30 | 14.43 | 342.8 | 0.66 | 0.81 |
| 60×60×3.5-240-FR | 250.6 | 0.30 | 15.00 | 388.1 | 0.32 | 14.36 | 315.6 | 0.65 | 0.79 |
| 80×80×3.5-320-F | 353.0 | 0.41 | 6.16 | 470.1 | 0.45 | 4.47 | 356.4 | 0.75 | 0.99 |
| 80×80×3.5-320-FR | 314.1 | 0.43 | 5.36 | 444.5 | 0.47 | 3.89 | 337.4 | 0.71 | 0.93 |
| 100×100×3.5-400-F | 440.8 | 0.55 | 2.12 | 520.5 | 0.60 | 1.54 | 397.5 | 0.85 | 1.11 |
| 100×100×3.5-400-FR | 437.6 | 0.55 | 2.15 | 529.0 | 0.60 | 1.56 | 404.0 | 0.83 | 1.08 |
| 120×120×8.0-450-F | 993.2 | 0.39 | 7.61 | 1145.0 | 0.39 | 7.27 | 908.8 | 0.87 | 1.09 |
| 120×120×8.0-450-FR | 841.1 | 0.40 | 6.64 | 1049.2 | 0.41 | 6.34 | 833.7 | 0.80 | 1.01 |
| 130×130×3.5-500-F | 437.4 | 0.81 | 0.90 | 564.5 | 0.88 | 0.85 | 410.6 | 0.77 | 1.07 |
| 130×130×3.5-500-FR | 414.8 | 0.80 | 0.91 | 561.0 | 0.87 | 0.86 | 408.3 | 0.74 | 1.02 |
| 150×150×3.5-600-F | 520.3 | 0.86 | 0.87 | 680.6 | 0.94 | 0.81 | 493.6 | 0.76 | 1.05 |
| 150×150×3.5-600-FR | 556.1 | 0.87 | 0.86 | 677.2 | 0.95 | 0.81 | 490.9 | 0.82 | 1.13 |
| 180×180×3.5-720-F | 528.1 | 1.05 | 0.75 | 718.0 | 1.15 | 0.70 | 517.0 | 0.74 | 1.02 |
| 180×180×3.5-720-FR | 468.1 | 1.04 | 0.75 | 732.9 | 1.14 | 0.70 | 527.8 | 0.64 | 0.89 |
| | | | | | | | Mean | 0.76 | 1.00 |
| | | | | | | | COV | 0.09 | 0.10 |

## FIGURES

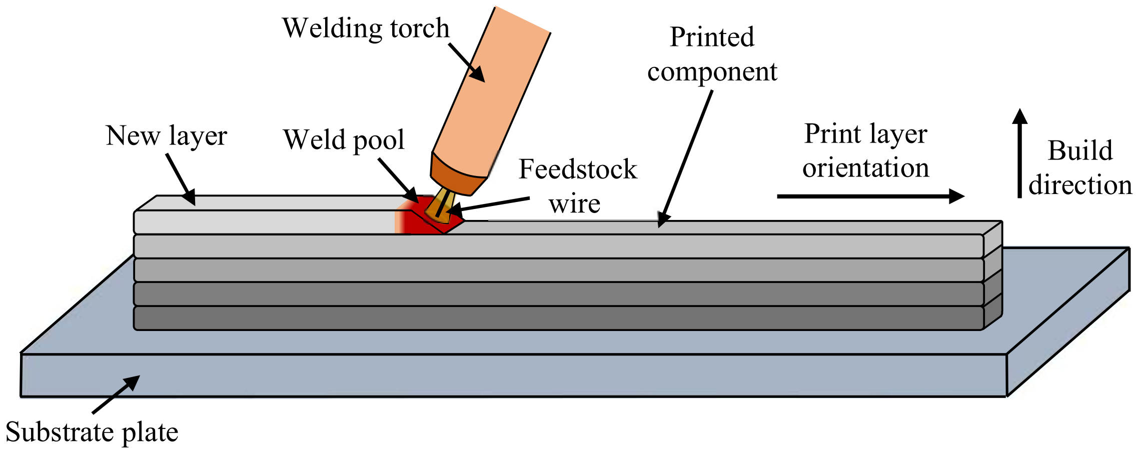


Figure 1: Illustration of the WAAM process

Figure 2: Overall view of MX3D Bridge (Gardner *et al*., 2020)

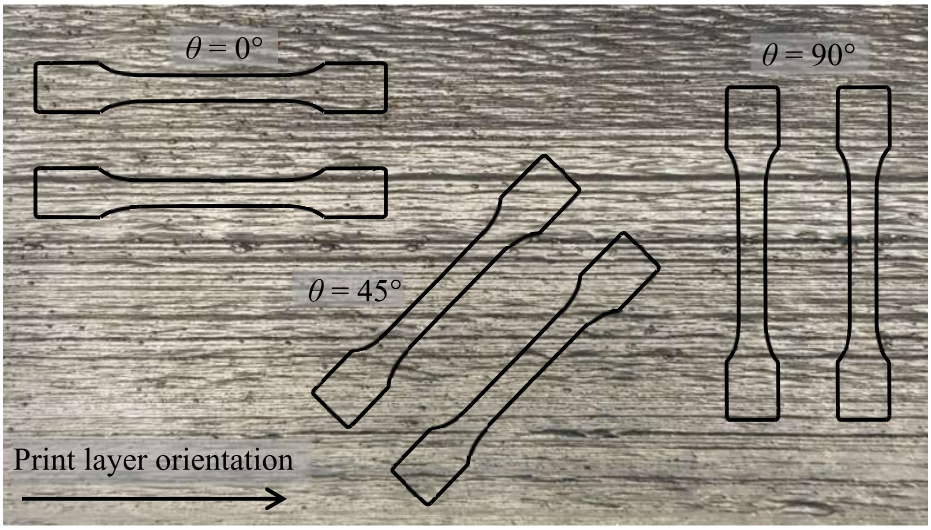


Figure 3: Orientation of tensile coupons extracted from WAAM plate relative to print layer orientation (Kyvelou *et al*., 2020)


Figure 4: Comparison between SHS specimen 120×120×8.0-450-F and its corresponding part of the MX3D Bridge (Gardner *et al*., 2020)

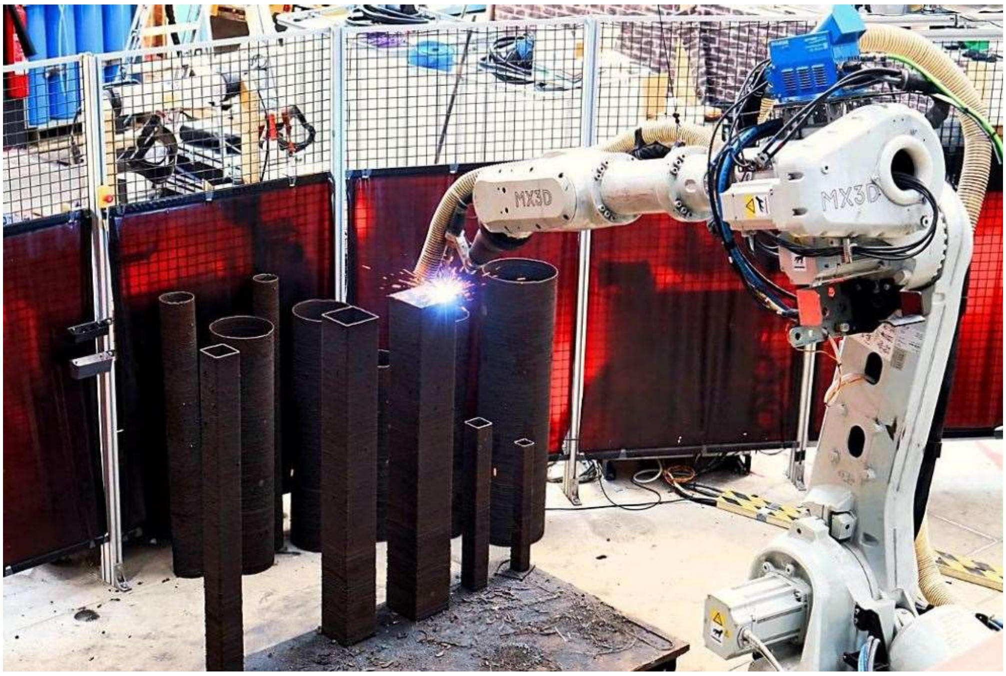


Figure 5: Printing of a subset of the SHS (and CHS) WAAM specimens

(a) Cutting using a band saw

(b) Sand-blasting with glass beads

Figure 6: Preparation of typical WAAM test specimen

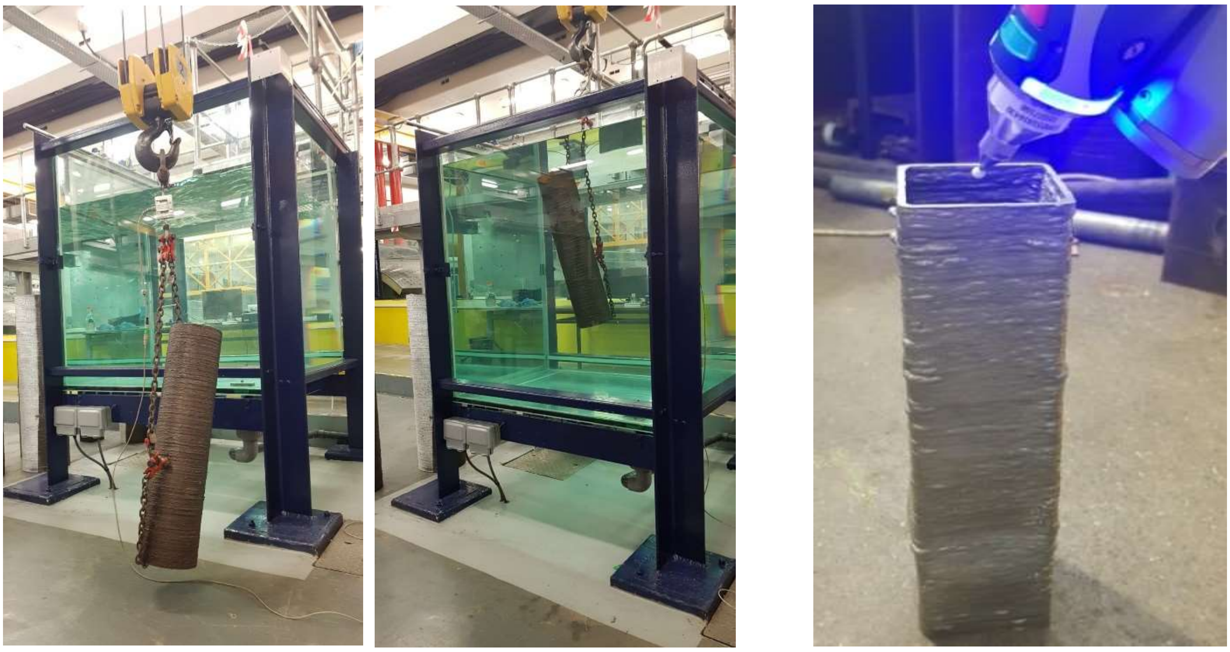

(a) Archimedes' measurements (shown for a CHS) (b) Laser scanning

Figure 7: Employed methods for geometrical measurements of WAAM stub columns

(a) Mixing silicone parts (b) Degassing

Figure 8: Preparation of silicone mixture

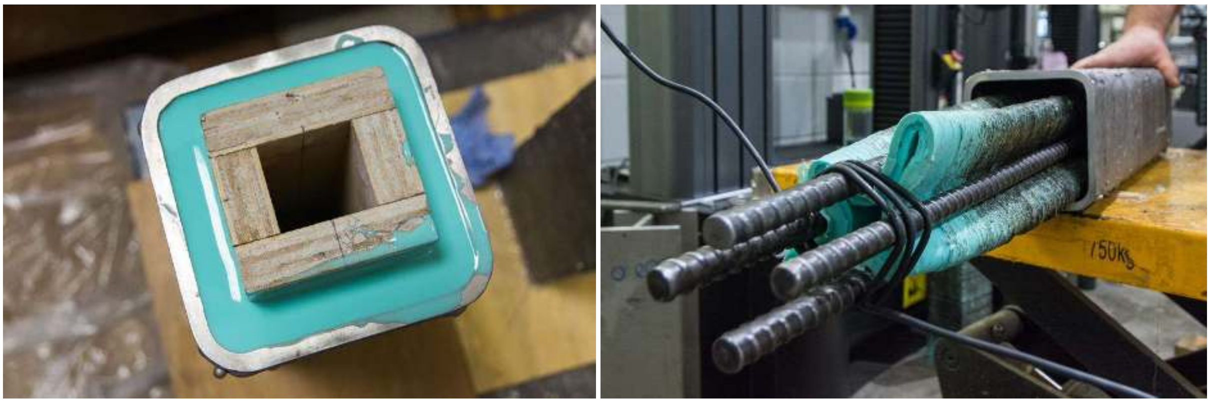

(a) Wooden insert within SHS (b) Removal of silicone cast from within the SHS

Figure 9: Process followed to produce silicone replicas of the inner surface of the SHS specimens

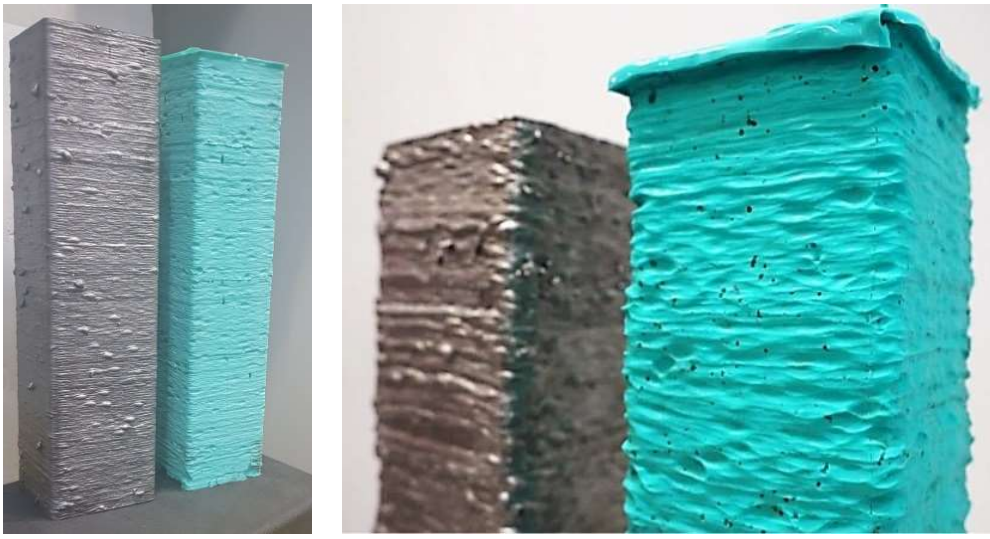

Figure 10: Silicone replica of the inner surface profile of typical SHS specimens

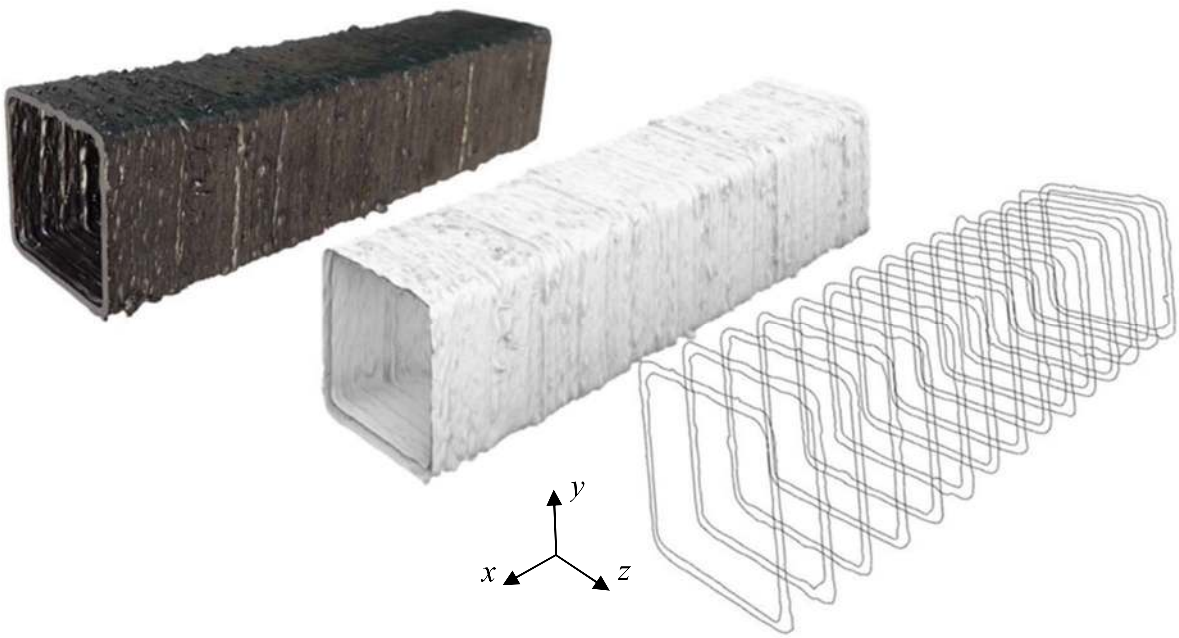


Figure 11: Specimen, 3D CAD model and cross-sectional contours of a typical SHS specimen

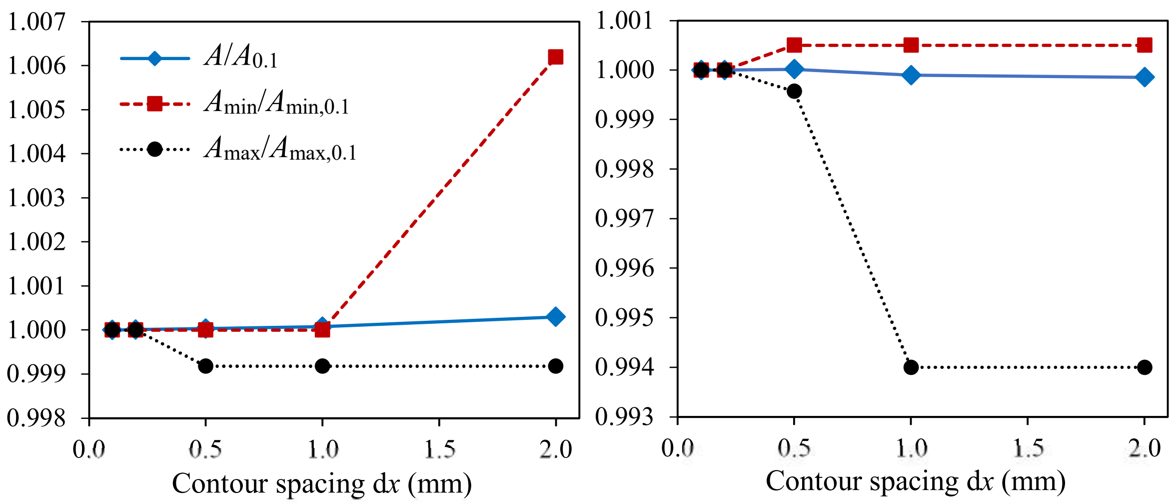


(a) 80×80×3.5-320-F (b) 80×80×3.5-320-FR

Figure 12: Results of sensitivity study on contour spacing

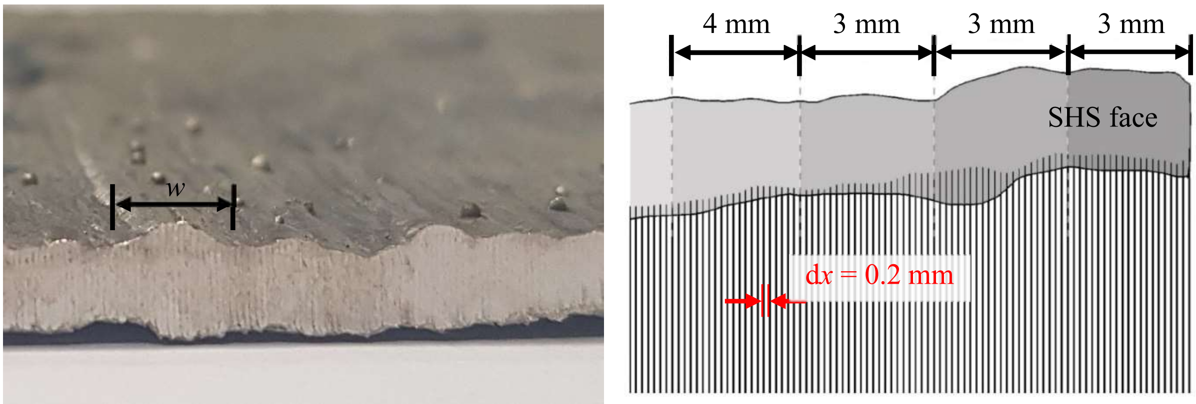


Figure 13: Typical deposition path widths compared to 0.2 mm contours

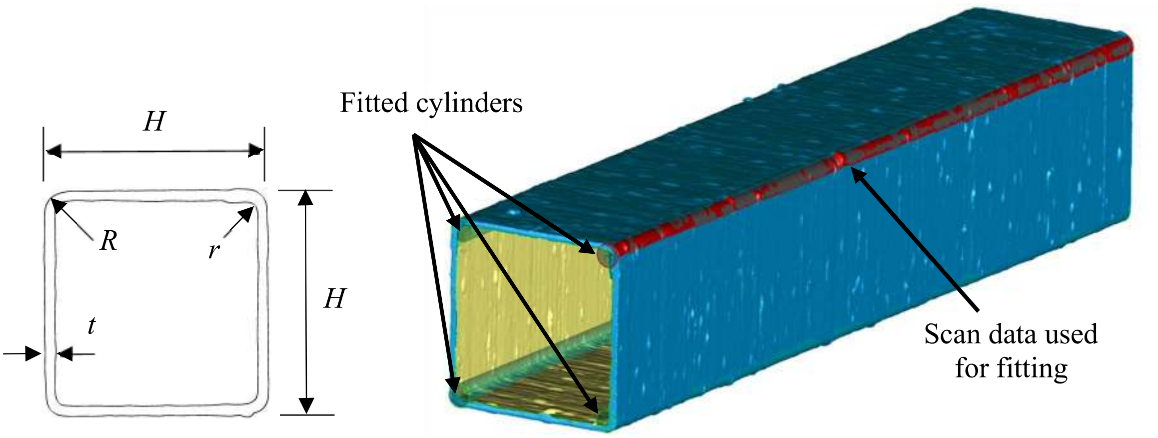


Figure 14: Cross-section geometry and derivation of the outer corner radius *R* from scanned data

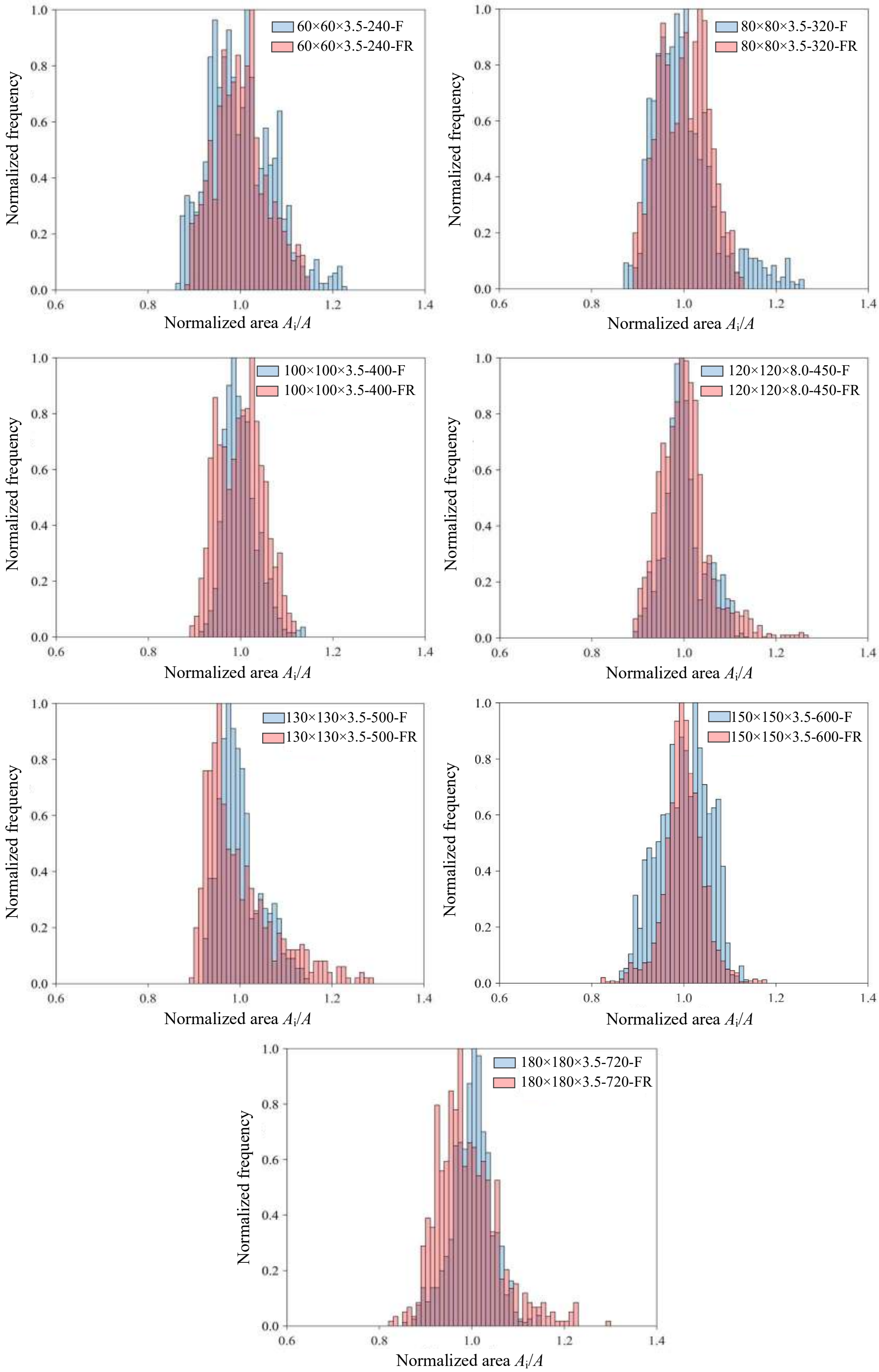


Figure 15: Distribution of normalized areas $A_i/A$ of examined specimens

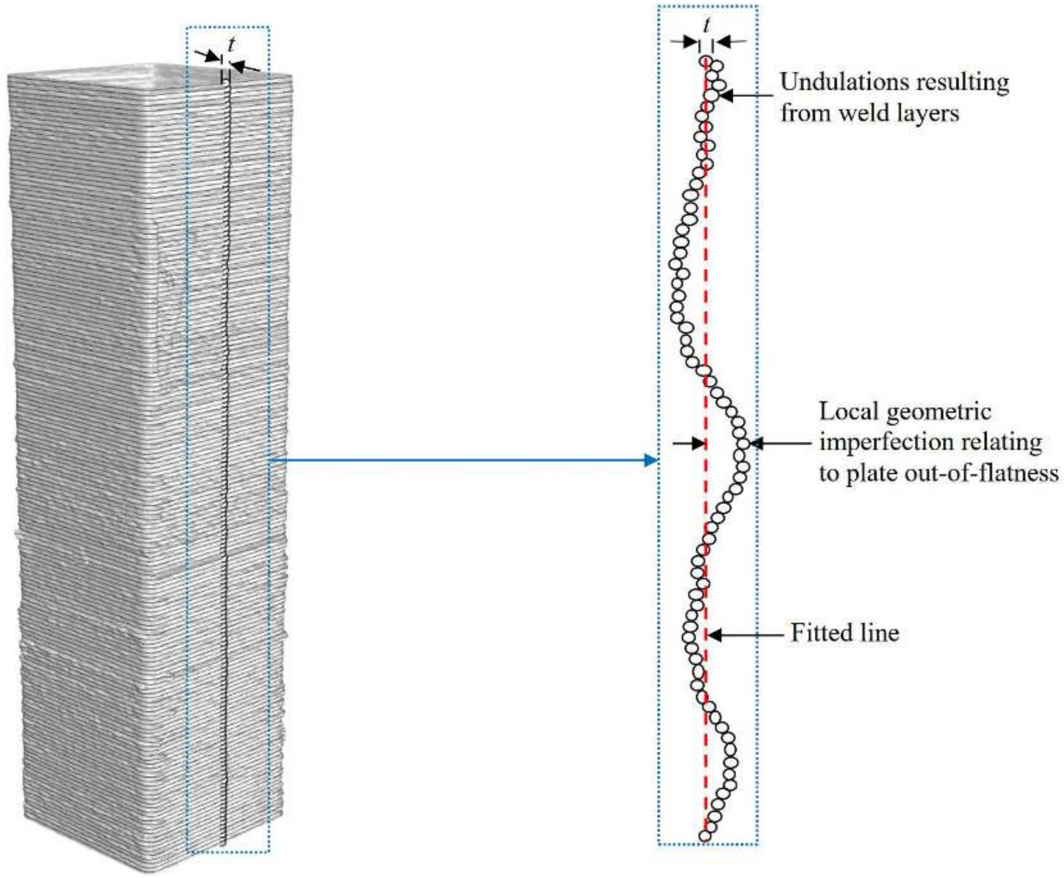


Figure 16: Distinction between surface undulations and local geometric imperfections

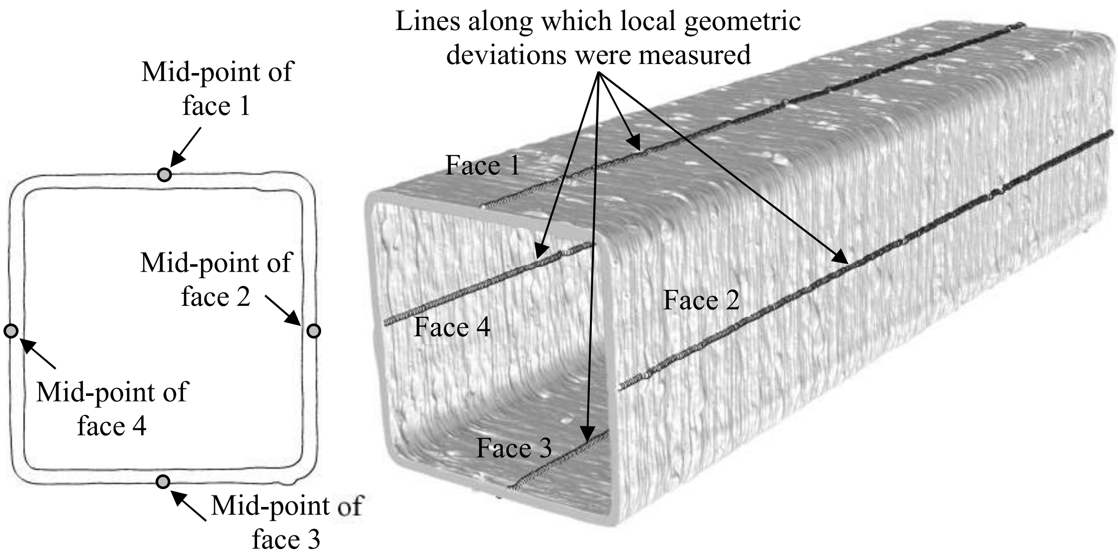


Figure 17: Determination of local geometric imperfections

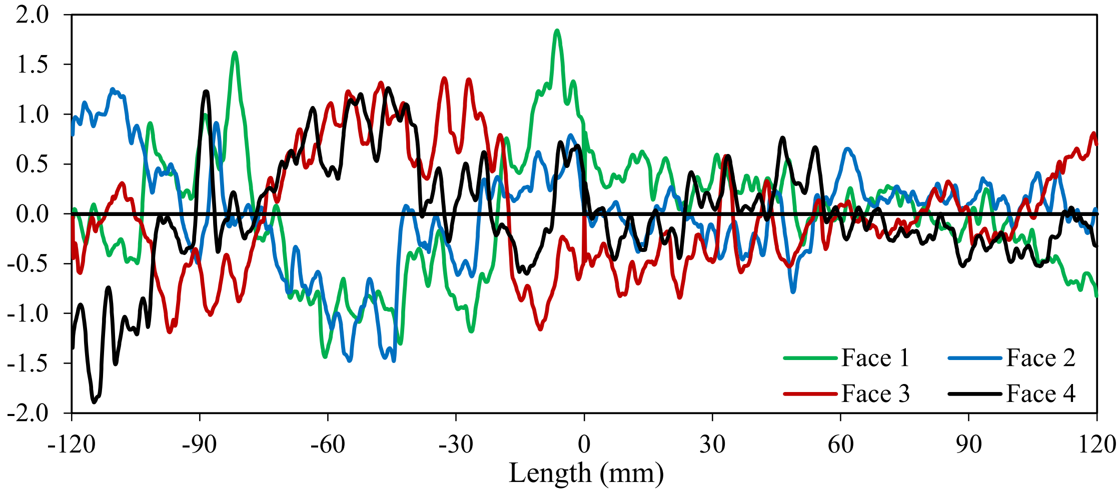


(a) Imperfection distributions before smoothing

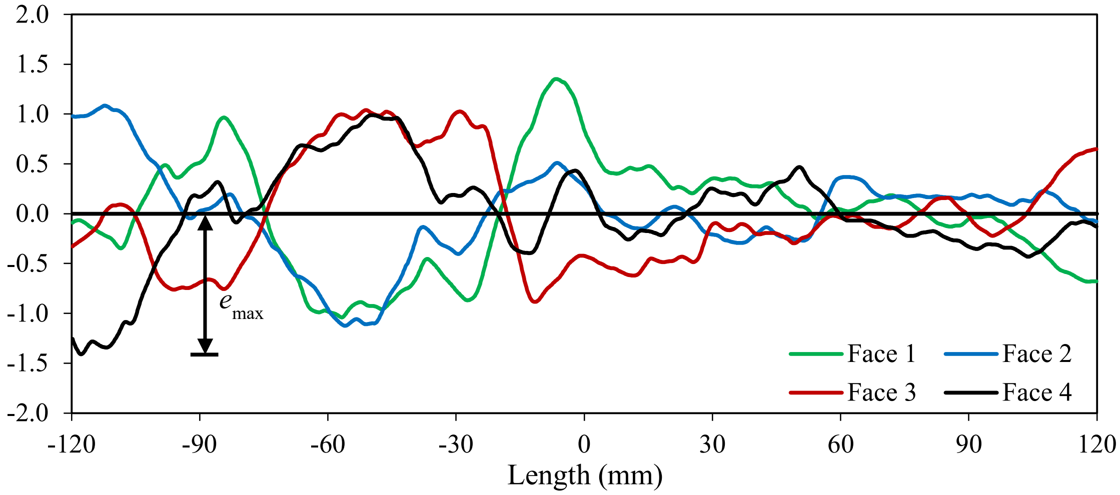


(b) Imperfection distributions after smoothing

Figure 18: Smoothing of local imperfection distributions to remove influence of unwanted features (e.g. weld beads) for a typical specimen (60×60×3.5-240-F)

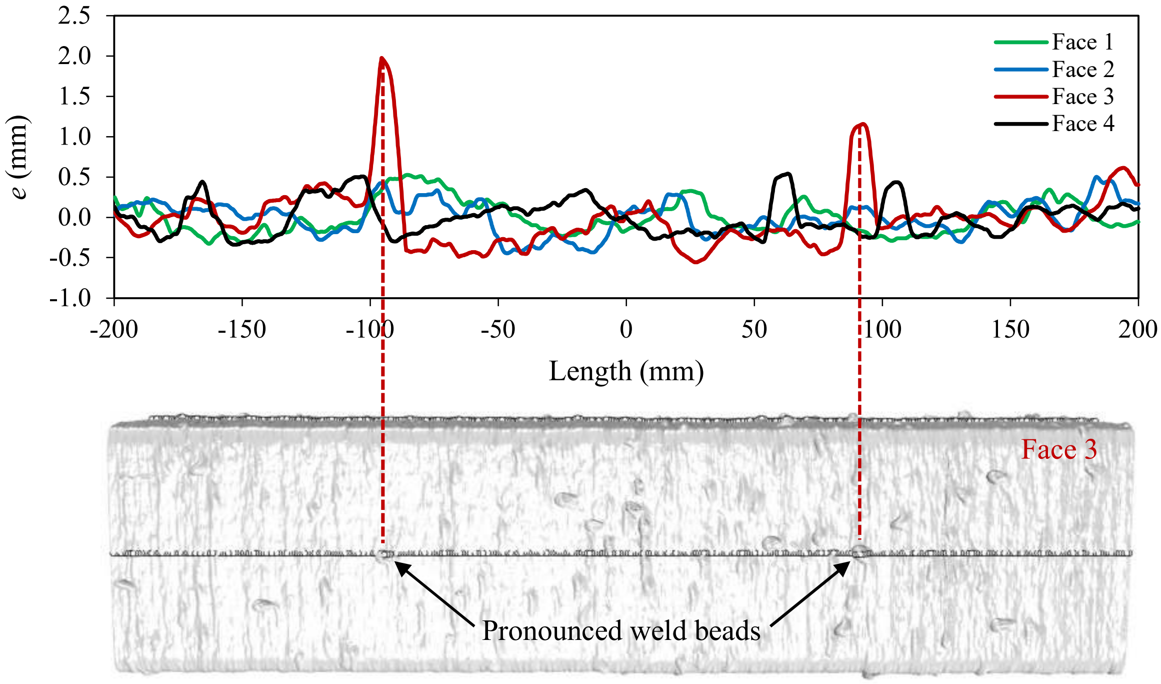


Figure 19: Measured local imperfection distributions for specimen 100×100×3.5-400-F

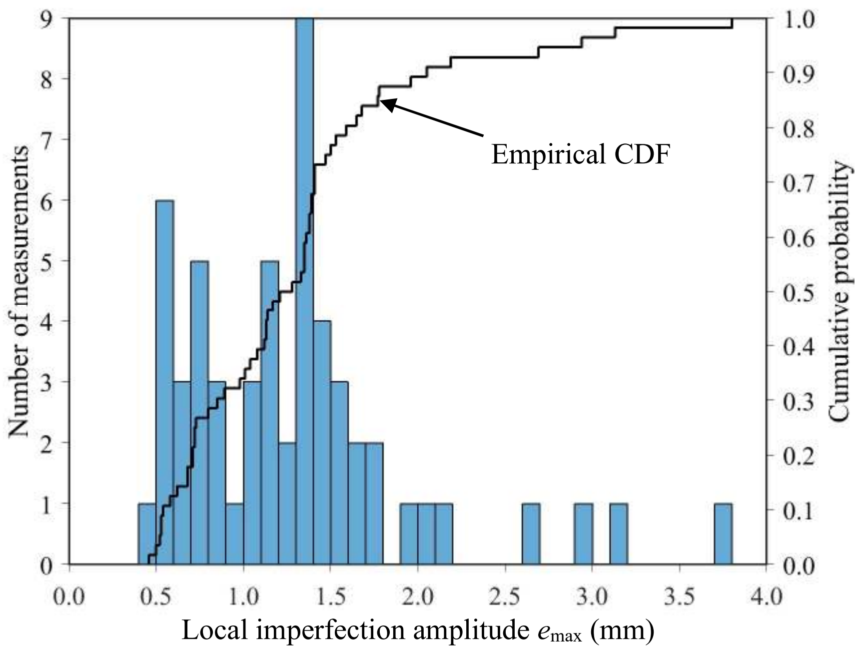


Figure 20: Histogram and CDF of local geometric imperfection amplitudes

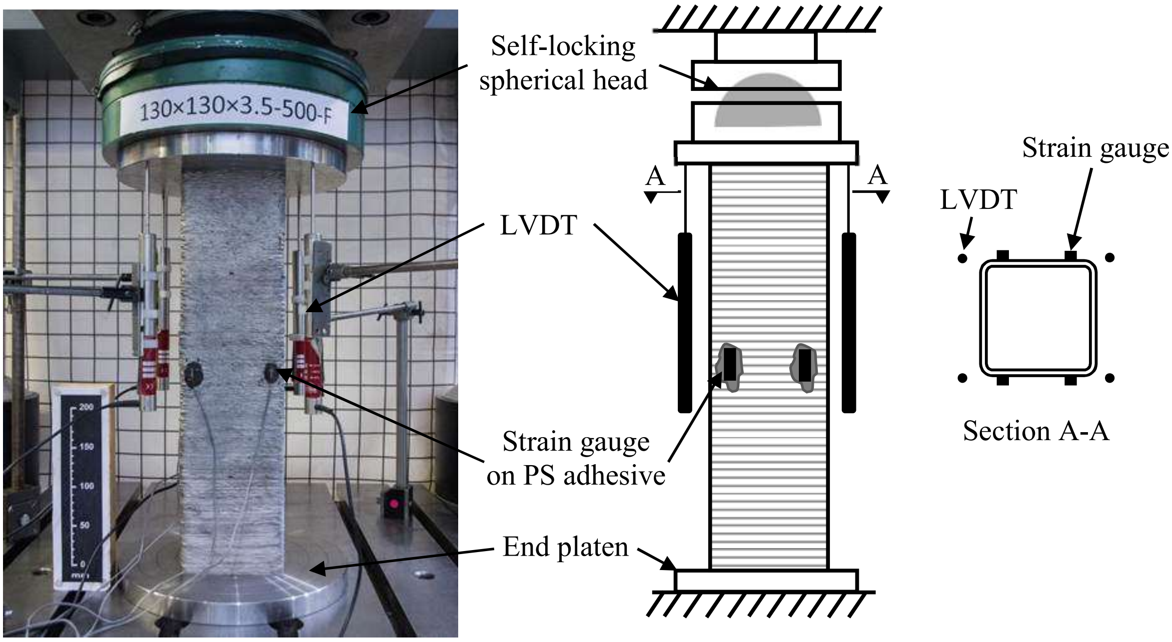


Figure 21: Experimental setup for stub column tests

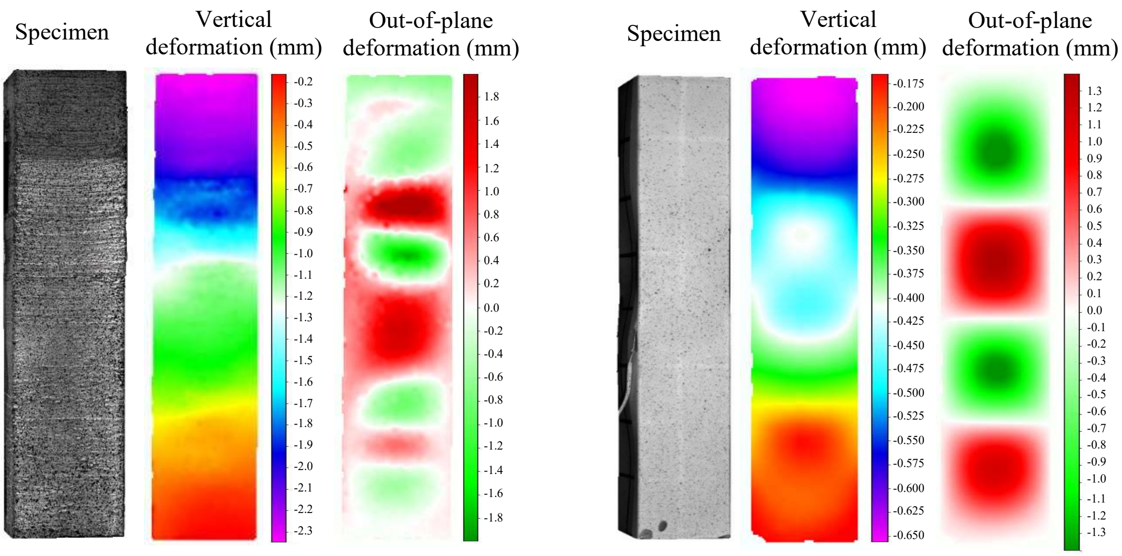


(a) WAAM SHS, $\bar{\lambda}_p$= 1.13 (180×180×3.5-720-FR)

(b) PBF SHS, $\bar{\lambda}_p$= 1.12

Figure 22: DIC analysis of typical WAAM and PBF specimens at ultimate load

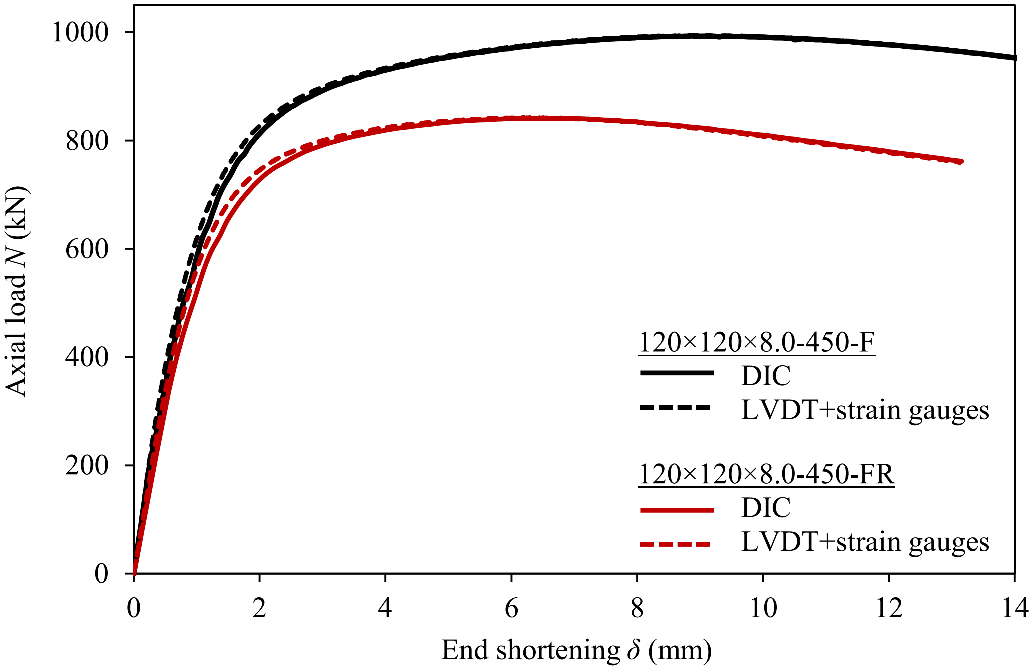


Figure 23: Typical comparisons of load-end shortening curves derived using DIC and LVDT+strain gauge data

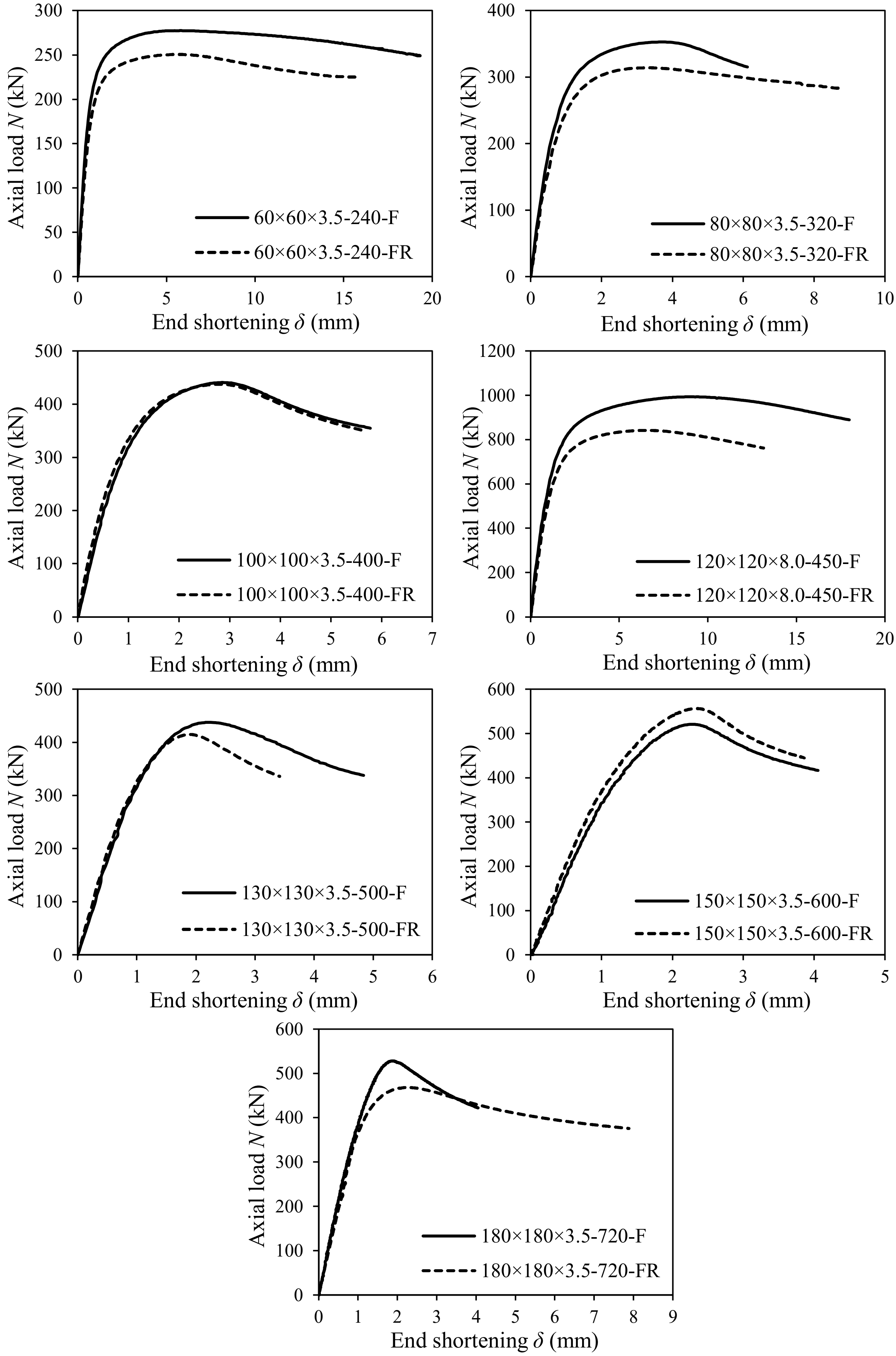


Figure 24: Load-end shortening curves of tested stub columns

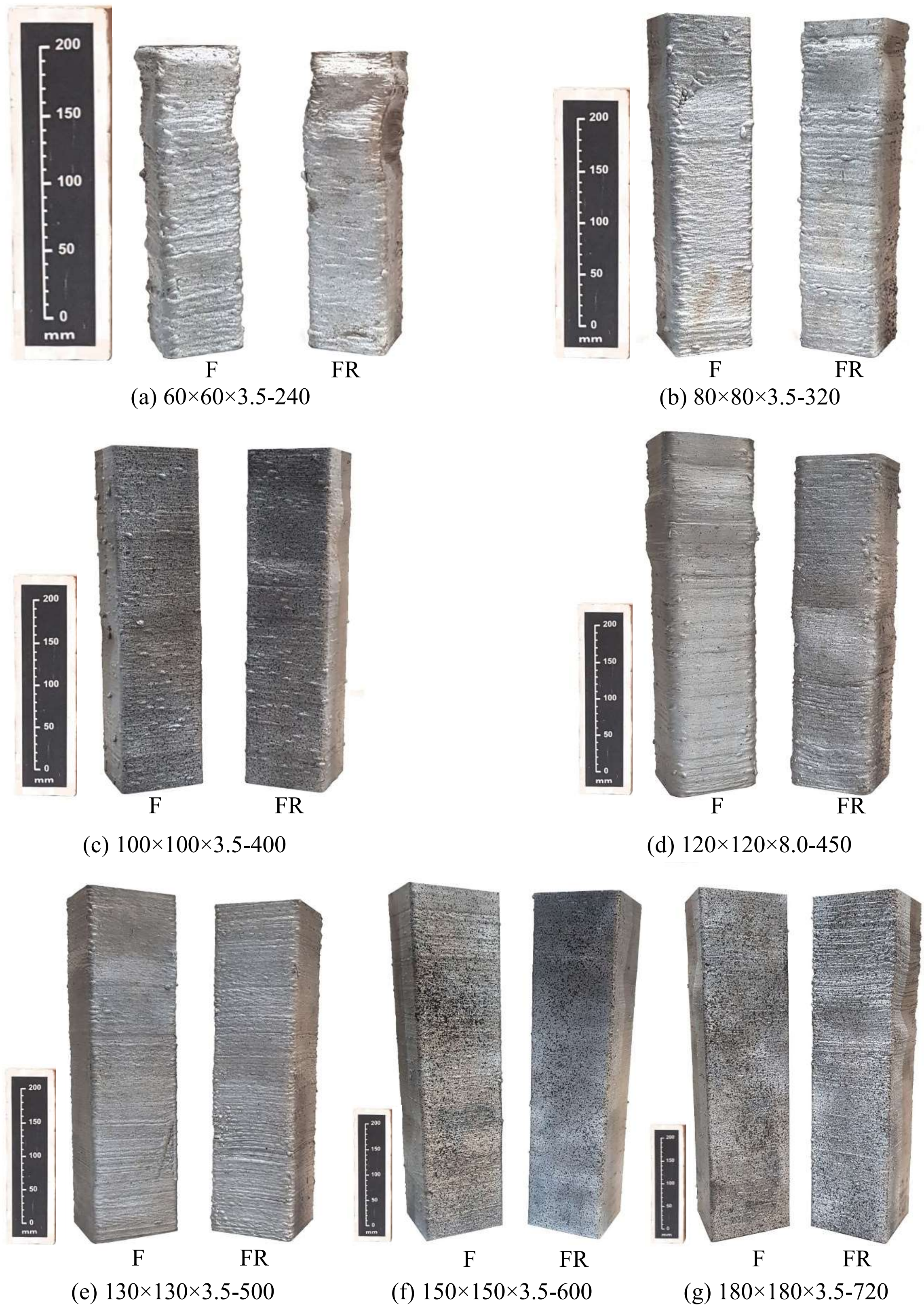


Figure 25: Deformed shapes of tested stub columns

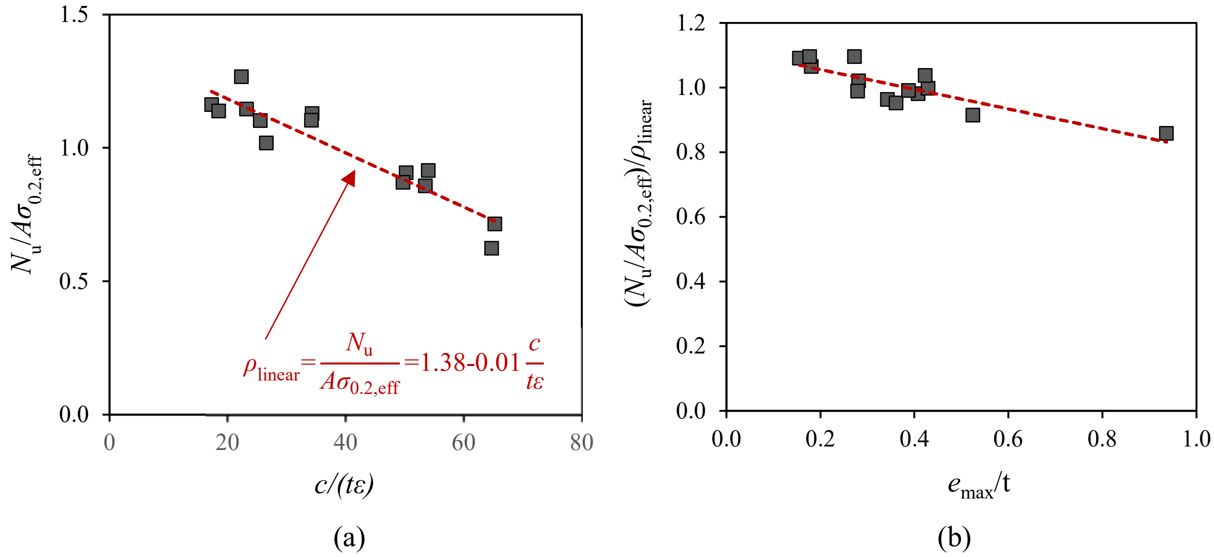


Figure 26: (a) Normalized compressive capacities of specimens and (b) variation of relative response of specimens with normalized geometric imperfection amplitude

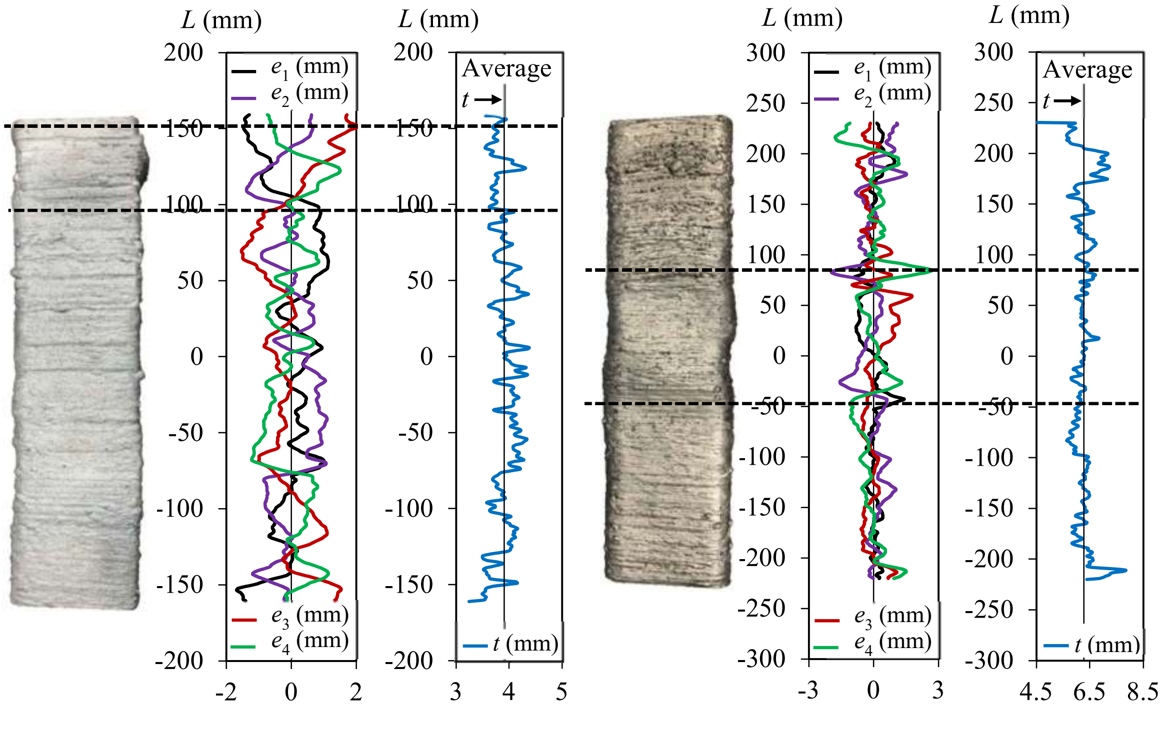


(a) Specimen 80×80×3.5-320-FR

(b) Specimen 120×120×8.0-450-FR

Figure 27: Correlation between geometric variability and failure locations for typical specimens of (a) 3.5 mm and (b) 8.0 mm nominal thickness

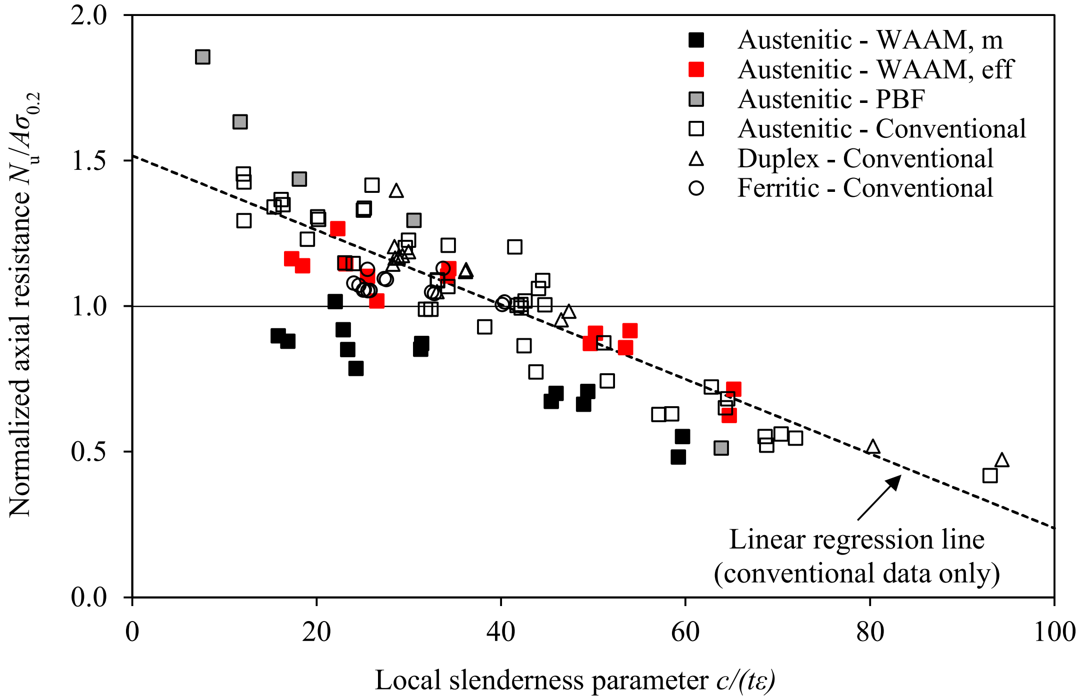


Figure 28: Comparison of normalized compressive capacities of WAAM SHS with those of PBF SHS and conventionally manufactured cold-formed SHS

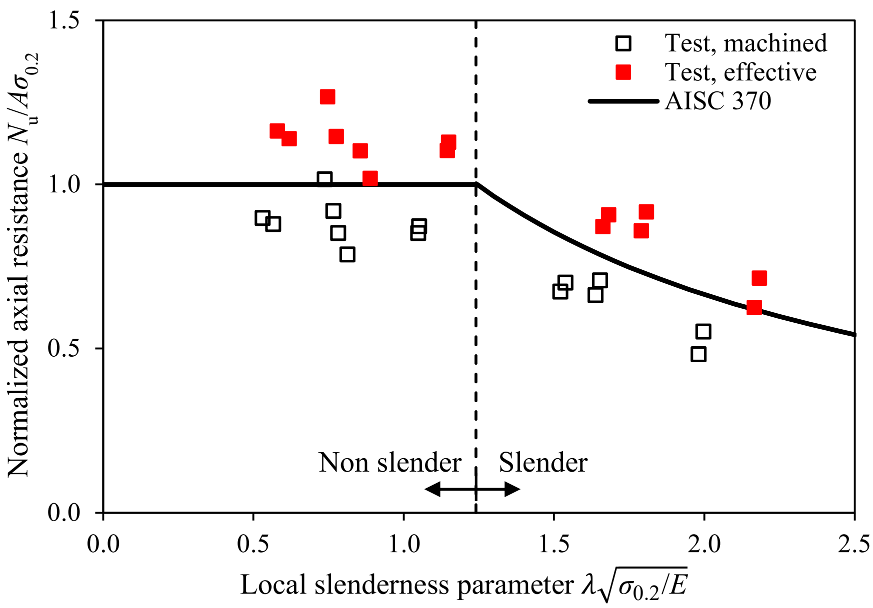


Figure 29: Comparison of compressive capacities of WAAM SHS with AISC 370 capacity predictions

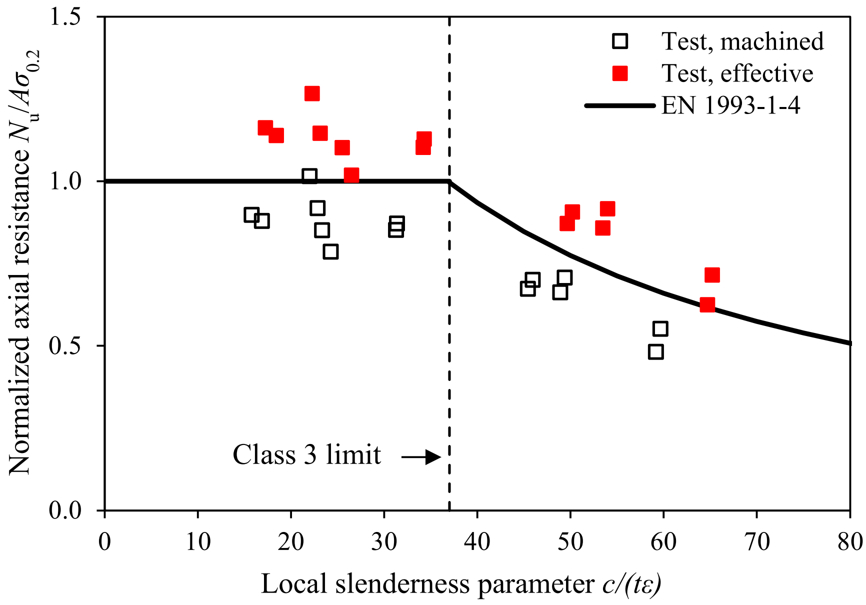


Figure 30: Comparison of compressive capacities of WAAM SHS with EN 1993-1-4 capacity predictions

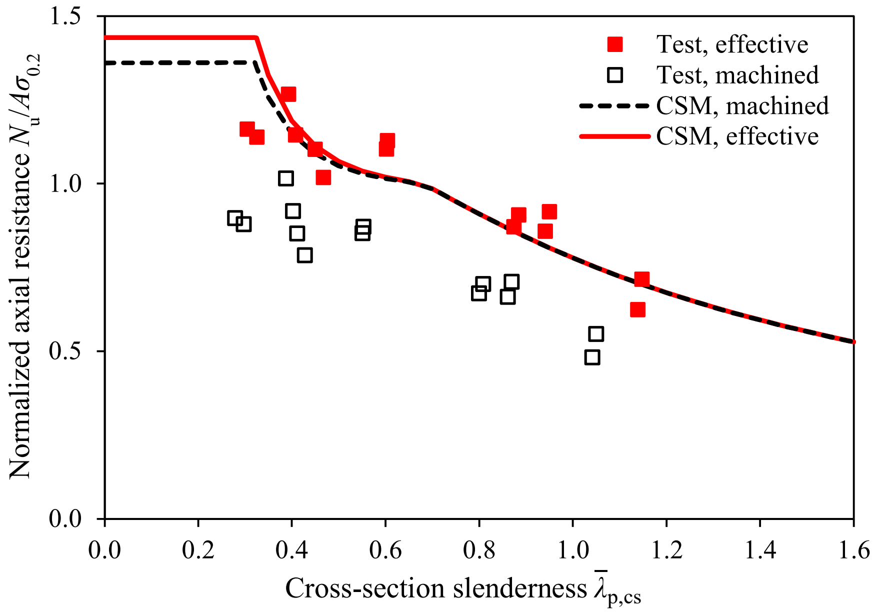


Figure 31: Comparison of compressive capacities of WAAM SHS with CSM capacity predictions